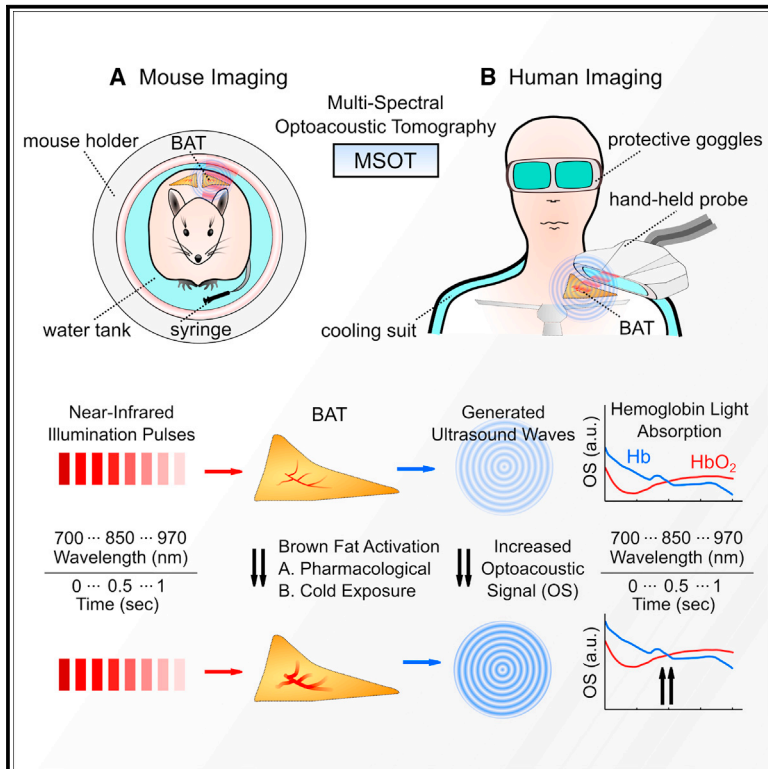


Cell Metabolism

Non-invasive Measurement of Brown Fat Metabolism Based on Optoacoustic Imaging of Hemoglobin Gradients

Graphical Abstract



Authors

Josefine Reber, Monja Willershäuser, Angelos Karlas, ..., Hans Hauner, Martin Klingenspor, Vasilis Ntziachristos

Correspondence

v.ntziachristos@tum.de

In Brief

Reber et al. employed label-free multi-spectral optoacoustic tomography to non-invasively image BAT and WAT in mice and humans and resolve BAT activation based on hemoglobin gradients. The 700–970 nm spectral range further enabled identification of BAT composition using lipid and water signatures.

Highlights

- MSOT enables hemoglobin-based detection of BAT activation in mice and humans
- MSOT images BAT composition label-free, based on hemoglobin, water, and lipid signal
- MSOT readouts of BAT activation correlate with indirect calorimetry
- Clinical MSOT detects BAT based on spectral absorption signatures



Non-invasive Measurement of Brown Fat Metabolism Based on Optoacoustic Imaging of Hemoglobin Gradients

Josefine Reber,^{1,2,9} Monja Willershäuser,^{3,4,5,9} Angelos Karlas,^{1,2} Korbinian Paul-Yuan,^{1,2} Gael Diot,^{1,2} Daniela Franz,⁶ Tobias Fromme,^{3,4} Saak V. Ovsepian,^{1,2} Nicolas Bézière,^{1,2} Elena Dubikovskaya,⁷ Dimitrios C. Karampinos,⁶ Christina Holzapfel,⁸ Hans Hauner,^{4,8,9} Martin Klingenspor,^{3,4,5} and Vasilis Ntziachristos^{1,2,10,*}

¹Institute for Biological and Medical Imaging (IBMI), Helmholtz Zentrum München, Neuherberg, Germany

²Chair for Biological Imaging, Technical University of Munich, Munich, Germany

³Chair of Molecular Nutritional Medicine, TUM School of Life Sciences, Technical University of Munich, Freising, Germany

⁴EKFZ – Else Kröner-Fresenius Center for Nutritional Medicine, Technical University of Munich, Freising, Germany

⁵ZIEL – Institute for Food and Health, Technical University of Munich, Freising, Germany

⁶Department of Diagnostic and Interventional Radiology, Technical University of Munich, Munich, Germany

⁷Department of Chemistry, Ecole Polytechnique Federale de Lausanne, Lausanne, Switzerland

⁸Institute for Nutritional Medicine, School of Medicine, Technical University of Munich, Munich, Germany

⁹These authors contributed equally

¹⁰Lead Contact

*Correspondence: v.ntziachristos@tum.de

<https://doi.org/10.1016/j.cmet.2018.02.002>

SUMMARY

Metabolism is a fundamental process of life. However, non-invasive measurement of local tissue metabolism is limited today by a deficiency in adequate tools for *in vivo* observations. We designed a multi-modular platform that explored the relation between local tissue oxygen consumption, determined by label-free optoacoustic measurements of hemoglobin, and concurrent indirect calorimetry obtained during metabolic activation of brown adipose tissue (BAT). By studying mice and humans, we show how video-rate handheld multi-spectral optoacoustic tomography (MSOT) in the 700–970 nm spectral range enables non-invasive imaging of BAT activation, consistent with positron emission tomography findings. Moreover, we observe BAT composition differences between healthy and diabetic tissues. The study consolidates hemoglobin as a principal label-free biomarker for longitudinal non-invasive imaging of BAT morphology and bioenergetics *in situ*. We also resolve water and fat components in volunteers, and contrast MSOT readouts with magnetic resonance imaging data.

INTRODUCTION

White adipose tissue (WAT) stores in its cellular fat droplets a surplus of vital energy consisting of macronutrients mainly in the form of triacylglycerides. In contrast, brown adipose tissue (BAT) works as a heater organ, utilizing the chemical energy extracted from carbohydrates and fat (Cannon and Nedergaard, 2004; Klingenspor, 2003). The presence of metabolically active

cervical, supraclavicular, and paravertebral BAT in adult humans has been discovered by the detection of high glucose-uptake rates using [¹⁸F]fluorodeoxyglucose positron emission tomography/computed tomography (¹⁸F-FDG-PET/CT) (Nedergaard et al., 2007; van Marken Lichtenbelt et al., 2009). In mice, BAT is located in several distinct depots in the cervical-thoracic and perirenal region and is utilized for non-shivering thermogenesis (Cannon and Nedergaard, 2004, 2011). The largest and most investigated BAT depot in rodents is the subcutaneous interscapular BAT (iBAT). It is densely vascularized and highly innervated by the sympathetic nervous system (Nnodim and Lever, 1988; Smith and Roberts, 1964). Research in small mammals has shown that cold exposure leads to the release of norepinephrine (NE) from nerve varicosities. The neurotransmitter NE stimulates β 3-adrenoreceptors located in the plasma membrane of brown adipocytes, resulting in the activation of the uncoupling protein 1 (UCP1) (Cannon and Nedergaard, 2004). UCP1 is expressed uniquely in brown adipocytes and upon activation facilitates a proton leak across the mitochondrial inner membrane, leading to the uncoupling of nutrient oxidation from ATP synthesis and thereby to heat generation (Klingenspor, 2003; Nicholls and Locke, 1984). BAT can also be activated via the subcutaneous or intravenous injection of sympathomimetics at the optimal dose, whereby the maximal increase above resting metabolic rate is used as a direct measure of BAT heating capacity (Golozoubova et al., 2001; Meyer et al., 2010). Sympathetic stimulation, however, not only activates BAT-induced non-shivering thermogenesis, but also increases energy expenditure at other sites, e.g., the cardiovascular system, potentially leading to an overestimation of BAT-induced thermogenesis (Cannon and Nedergaard, 2004).

The study of BAT physiology has attracted attention in recent years, due to the assumed association of BAT with a wide variety of human diseases such as obesity (low BAT activity), diabetes (absence of active BAT), cachexia (high amount and activity of BAT), and atherosclerosis (atheroprotective role of BAT and



similar perivascular fat) (Bauwens et al., 2014). Classic studies obtained snapshots of BAT metabolic activity by measurements of blood flow, as assessed by injecting radiolabeled particles, and arterio-venous differentials in blood oxygenation (Foster and Frydman, 1978, 1979; Puchalski et al., 1987). Non-invasive ^{18}F -FDG-PET imaging resolves glucose-uptake rates in living tissue but underestimates metabolic activity of BAT (Bauwens et al., 2014; Mirbolooki et al., 2011), since thermogenesis is largely fueled by mitochondrial beta-oxidation of fatty acids. [^{18}F]Fluoro-6-thia-heptadecanoic acid and ^{11}C -acetate may address this issue (see, e.g., Ouellet et al., 2012), but the use of radio-isotopes does not allow continuous or longitudinal studies and is problematic for human measurements. Studies with functional magnetic resonance imaging (MRI) (Chen et al., 2012) or near-infrared (NIR) fluorescence imaging (Nakayama et al., 2003) have provided observations of blood flow associated with BAT activation but did not accurately differentiate BAT from WAT. Likewise, infrared imaging has been considered for resolving local temperature changes after BAT activation (Crane et al., 2014), but it provides 2D surface-only views of volumetric temperature changes within the examined tissue volume that challenge quantification and accurate insights into the underlying activity. The study of BAT and other tissue metabolism could be revolutionized by methods that offer non-invasive and point-of-care longitudinal measurements of activity, avoiding radioactivity or the use of targeted contrast agents and expensive scanners and infrastructure. Such technology could promote the disseminated investigation of metabolism in BAT and other tissue over time and in response to external natural stimuli or new anti-obesity drugs in animals and humans in a personalized manner.

We investigated label-free non-invasive imaging of BAT activation and tissue metabolic activity based on real-time NIR optoacoustic sensing of hemoglobin. Label-free imaging based on non-ionizing energy avoids the use of contrast agents and opens up the possibility for frequent and longitudinal measurements in individual subjects. A primary hypothesis in the study was that BAT activation could be measured by resolving hemoglobin oxygenation gradients, representative of local oxygen utilization and blood influx.

To validate hemoglobin gradients as a marker of energy expenditure, we developed an experimental arrangement that concurrently collected multi-spectral optoacoustic tomography (MSOT) and breathing gas data from mice and humans, using indirect calorimetry (IC). Necessary imaging performance was achieved based on a unique imaging sequence, which collected one cross-sectional optoacoustic image per laser pulse and per wavelength at 10 Hz frame rates over a 700–970 nm spectral range. Up to 28 illumination wavelengths per MSOT frame were collected. Previously undisclosed correlation of IC with *in situ* MSOT measurements of BAT metabolic changes was performed in mice and pilot studies in humans. Human findings were further corroborated using ^{18}F -FDG-PET.

In addition to BAT activation studies, we investigated the morphological discrimination between BAT and WAT in healthy and diabetic mice as well as the effect of β 3-adrenergic remodeling of WAT. While hemoglobin can be unmixed in the 700–900 nm range, MSOT operation in the extended 900–970 nm range further computed tissue fat and water

components in human volunteer studies and observed tissue composition differences in BAT and WAT, contrasted with MRI of the same volunteers. We discuss how MSOT demonstrates capacities in metabolic imaging that are unattainable by any other imaging modality today, offering a paradigm shift in the study of metabolic processes in living tissue. Shown correlations between MSOT measurements of local metabolic activity and IC measuring whole-body metabolic profiles may have broad implications in metabolism research and clinical applications in obesity, diabetes, atherosclerosis, and related fields.

RESULTS

Optoacoustic Differentiation of BAT from WAT

We interrogated whether iBAT and inguinal WAT (ingWAT) can be spectrally differentiated. We were particularly interested in NIR measurements that allow light penetration several millimeters to centimeters deep into tissue. Excised iBAT and ingWAT from mice were placed next to an India ink reference tube in a scattering (non-absorbing) holder and measured by NIR-MSOT under identical conditions (Figure 1A; see experimental arrangement in Figure S1A). At 800 nm the mean pixel intensity of the 2D transverse optoacoustic image of iBAT was 103 ± 13 a.u., whereby ingWAT was at 42 ± 7 a.u. and the reference absorber at ~ 64 a.u. in all measurements. Comparing the spectra of iBAT, ingWAT, and black India ink (OD = 0.5 at 800 nm), iBAT showed the overall highest signal intensity (light absorption) with a local maximum at 750 nm and a minimum at 830 nm. ingWAT has a maximum at 740 nm and a minimum at 800 nm. As expected, India ink demonstrated the highest absorption in the 700 nm region and a gradual absorption decrease toward 900 nm (Figure 1B).

To inquire whether iBAT can be separated from ingWAT and other surrounding tissues *in vivo*, we imaged nude mice by MSOT in the NIR range (700–900 nm). iBAT is typically localized in the cervical-thoracic region as shown in an anatomical transverse cryoslice (Figure 1C) obtained by white-light (color) imaging of cryoslices from a mouse enrolled in the MSOT imaging study. The iBAT depot resides between the shoulder blades of the animal in a bilateral symmetrical arrangement, on the left and right of the body axis. Mice were anesthetized using pentobarbital, which has no inhibitory effects on BAT thermogenesis (Chen et al., 2012; Granneman et al., 2003), in contrast to isoflurane and other inhalation anesthetics, including halothane (Dicker et al., 1995; Ohlson et al., 1994, 2003). An optoacoustic image at 800 nm exhibited areas with strong absorption (Figure 1D) that were congruent with the areas identified as iBAT in the corresponding cryoslice (Figure 1C). The ingWAT spectrum collected *in vivo* is flat compared with the iBAT spectrum also *in vivo* (Figure 1E); the latter has a minimum at 760 nm and a maximum at 800 nm. In addition to the spectral differences, iBAT exhibits a stronger optoacoustic signal than surrounding tissues *in vivo*, which allows the visualization of iBAT even at a single wavelength. Thus, the results demonstrate that MSOT can differentiate BAT and WAT morphology *ex vivo* and *in vivo*. MSOT also allowed the anatomical capture of the Sulzer vein (SV; Figure 1D, black square; see also Figures 2A and 3A), representing the main venous drainage of iBAT.

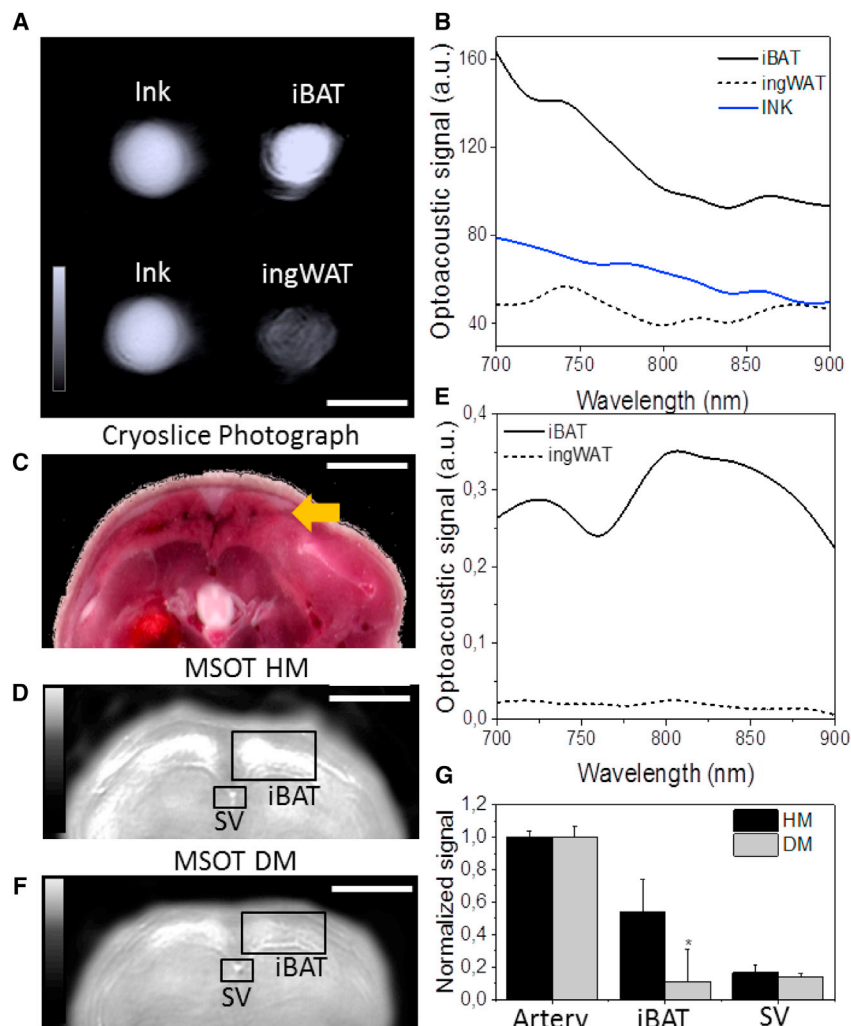


Figure 1. Ex Vivo and In Vivo Comparison of the Optoacoustic Signal Generated from iBAT and ingWAT

(A) Reconstructed optoacoustic images of excised iBAT and ingWAT from paraformaldehyde-perfused animals and ink (OD = 0.5 at 800 nm) measured at 800 nm in scattering phantom.

(B) Optoacoustic spectra of *ex vivo* iBAT, ingWAT, and ink in the NIR as measured by MSOT.

(C) Anatomical transverse cryoslice of the neck area showing iBAT (arrow).

(D) Reconstructed MSOT image (800 nm) showing iBAT and the Sulzer vein (SV) *in vivo* (black squares). HM, healthy mouse.

(E) Optoacoustic spectra of *in vivo* iBAT and ingWAT in the NIR region as measured by MSOT.

(F) Reconstructed MSOT image (800 nm) of diabetic mouse (DM) *in vivo*.

(G) Normalized signal of MSOT image (800 nm) in a reference artery, the iBAT, and the SV in HM and DM. Scale bars, 3 mm (A), 1 cm (C, D, and F). * $p < 0.05$. Data are represented as mean \pm SEM.

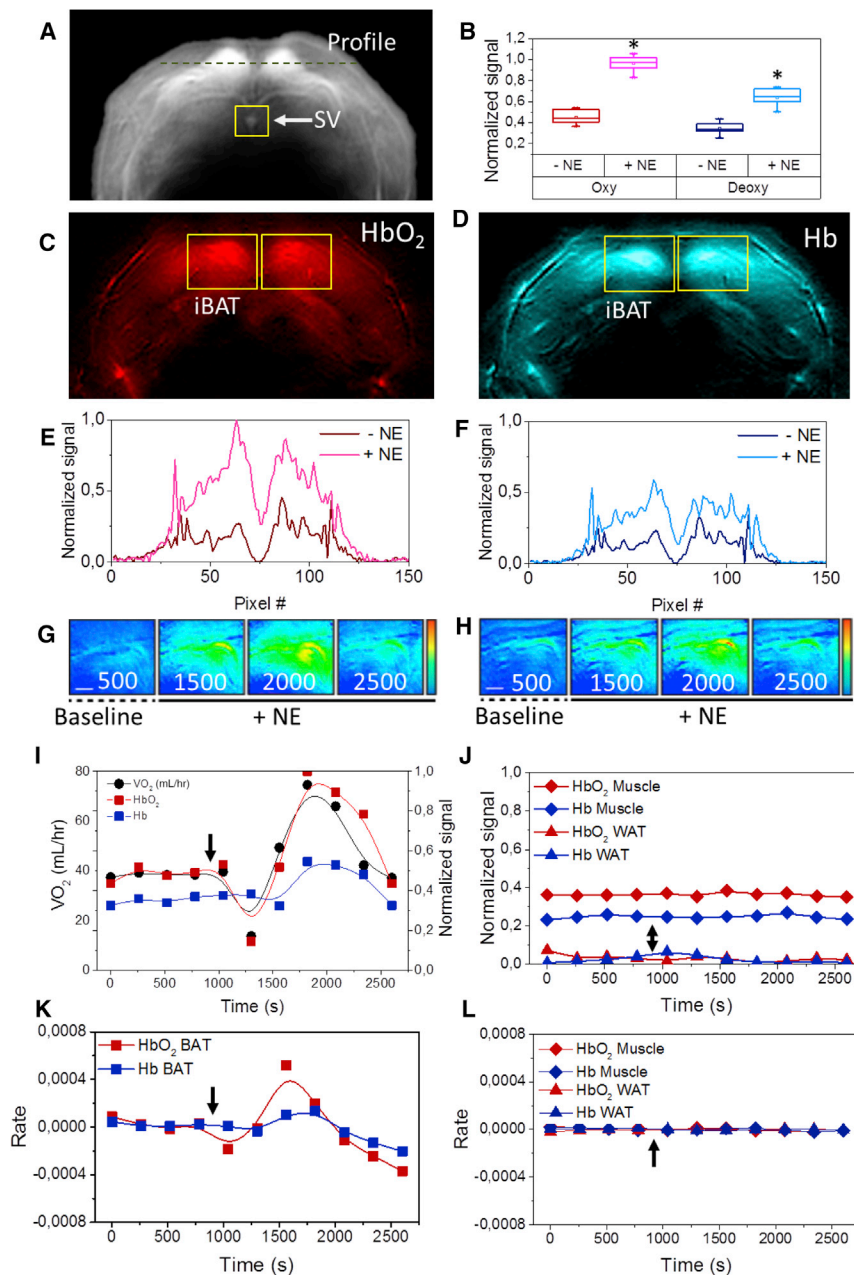
performing, for the first time reported, a correlation of hemoglobin-based optoacoustic readings with concurrent IC measurements based on breathing gas analysis (FoxBox, Sable Systems International) (Figure S1A). iBAT activation was induced in nude mice ($n = 6$) by intravenous administration (1 mg/kg) of NE.

Baseline (pre-NE, NE $-$) and iBAT activation (post-NE, NE $+$) MSOT images were recorded over a period of 42 min with a step of ~ 4 min, resulting in four iBAT pre-NE scans and seven post-NE scans. At baseline, MSOT clearly identified two bilaterally symmetrical iBAT locations (Figure 2A),

which were subsequently employed to define ROIs for HbO₂ and Hb calculations. Unmixed HbO₂ (Figure 2C) and Hb (Figure 2D) images identified mean HbO₂ intensity of the iBAT ROI of 0.45 ± 0.07 (NE $-$) prior to activation and 0.96 ± 0.08 (NE $+$) after activation ($p < 0.0001$). The Hb signal intensity increased significantly from 0.34 ± 0.06 (NE $-$) to 0.64 ± 0.08 (NE $+$) ($p < 0.0001$) (Figure 2B). As in the experiments above, values are referenced to an artery signal, i.e., to a 100% HbO₂ signal. Intensity profiles drawn through the iBAT regions along the cross-sectional black dashed line marked with the term “profile” in Figure 2A demonstrated intensity differences between baseline and activated states for the bilateral iBAT lobes, but not for surrounding tissues (Figures 2E and 2F). Area under the curve (AUC) calculations for the HbO₂ profiles (Figure 2E) identified an AUC change from 30.8 ± 6.1 (NE $-$) to 63.6 ± 2.6 (NE $+$) after activation ($p = 0.007$). The AUC of the Hb profile (Figure 2F) was 20.1 ± 3.7 (NE $-$) before and 39.2 ± 1.8 (NE $+$) after activation ($p = 0.027$). To quantify the spatial topology of the activation, we drew contour maps (Figures S3A and S3C) of the HbO₂ and Hb spatial patterns observed *in vivo* for the ROI. The contours quantify the areas implicated in the activation and demonstrate a 3.6-fold mean increase in high-intensity areas for HbO₂

In Vivo Imaging of iBAT Activation in Mouse

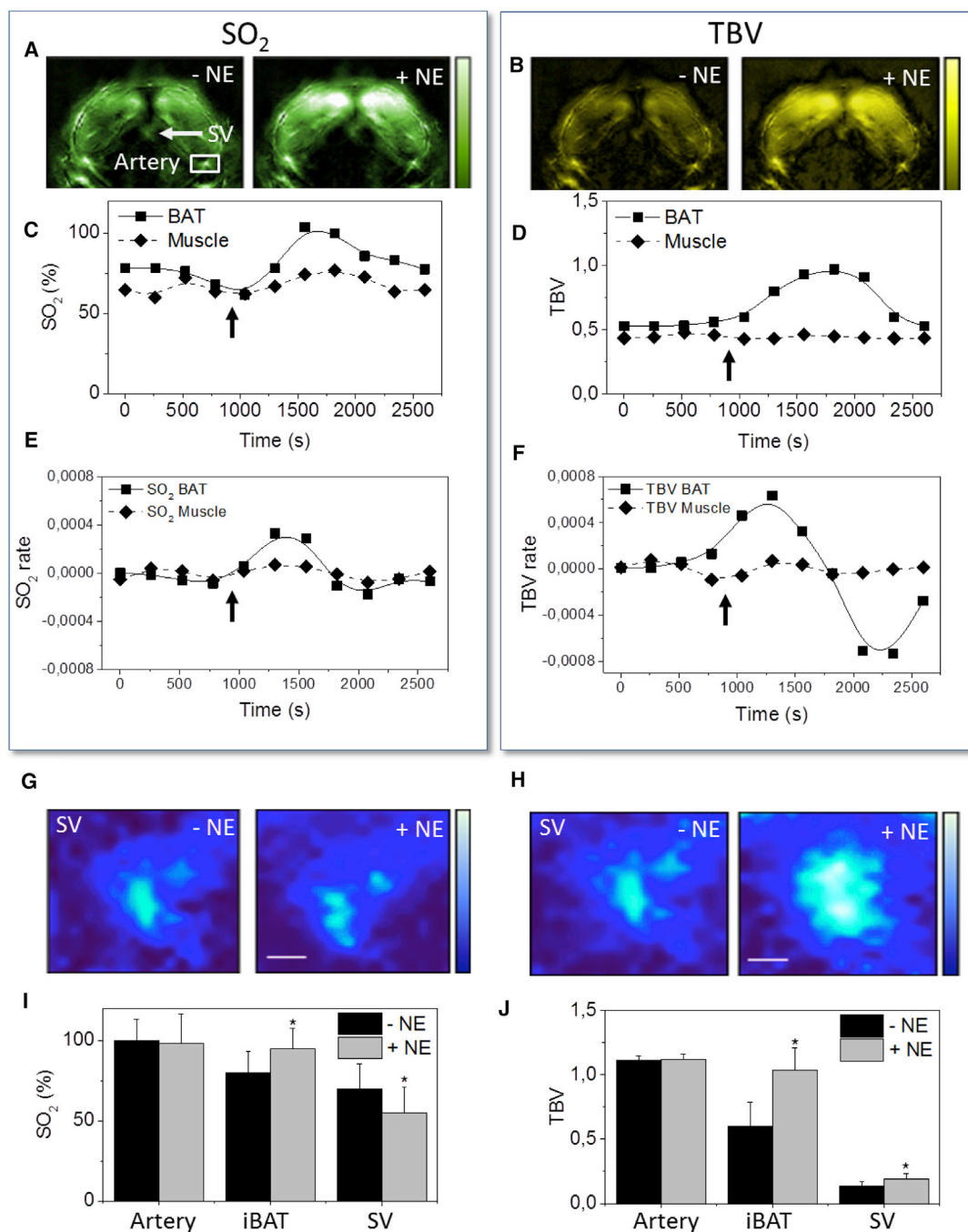
Next, we examined the possibility of interrogating iBAT activation in healthy mice based on measurements of HbO₂ and Hb gradients, hypothesized herein as an intrinsic biomarker of metabolism. We developed a novel experimental platform for



and a 2.1-fold mean increase for Hb within iBAT between pre-NE and post-NE measurements for the mice examined (Figure S3).

Longitudinal imaging of the iBAT clearly resolved changes in HbO₂ and Hb signals during activation (Figures 2G and 2H), which were compared with oxygen consumption ($\dot{V}O_2$) measured by IC over time (Figure 2I). The HbO₂ and $\dot{V}O_2$ responses showed a similar time pattern, whereas changes in the Hb signal appeared in a delayed fashion. The HbO₂ signal initially dropped post-NE administration, indicating a surge of oxygen utilization, whereas the Hb signal exhibited only a small change. At 650 s after NE administration, there is a prominent increase in both HbO₂ and Hb signals, indicating a blood volume increase (blood flow/perfusion) in the activated iBAT area, which reached a maximum at ~900 s post-activation. Similar to the HbO₂ signal,

as the NE injection, showed no significant difference ($\dot{V}O_2$, 42 ± 4 mL/hr at baseline and 43 ± 5 mL/hr post-injection, *p* = 0.3; HbO₂, 0.43 ± 0.04 at baseline and 0.49 ± 0.11 post-injection, *p* = 0.3; Hb, 0.35 ± 0.03 at baseline and 0.36 ± 0.05 post-injection, *p* = 0.5) (Figures S3E and S3F). We further studied the derivative of HbO₂ and Hb (Figures 2K and 2L), which indicates the rate of change in blood constituent levels, reflecting their utilization and transport in tissue. The maximum HbO₂ rate occurred at 650 s and the maximum Hb rate at 850 s after activation. The correlation between hemoglobin and IC measurements confirms the original hypothesis that high-resolution images of HbO₂ and Hb reflect BAT activation. However, in contrast to IC measurements, MSOT readings allow *in situ* observations along with the visualization of the metabolically activated area.



Saturation and Blood Volume Rates

The sum of HbO₂ and Hb, defined as total blood volume (TBV), and the fractional contribution of HbO₂ normalized against the TBV, i.e., the blood oxygen tissue saturation (SO₂), were also calculated based on MSOT images (Figures 3A and 3B) and are shown here to have a different time response compared with their Hb and HbO₂ constituents. After NE administration, iBAT SO₂ initially decreases, possibly because of higher metabolic demand, and then increases to a maximum at ~800 s post-NE (Figure 3D). TBV follows a similar trend, starting to increase at ~900 s post-NE (Figures 3C and 3D). Time derivatives of SO₂ and TBV values were also computed, since while SO₂ values indicate the amount of HbO₂ in the TBV present in tissue, the rate of SO₂ change reflects more closely the oxygen demand by tissue, i.e., oxygen utilization. Observation of the SO₂ rate (time derivative; Figure 3E) indicates an increase in oxygen demand (metabolism) immediately after NE activation, which intensifies in the subsequent ~700 s post-activation. The TBV rate (Figure 3F) also indicates an increased demand in blood volume and is representative of the blood volume influx, i.e., flow or perfusion.

To independently assess oxygen utilization, we spectrally resolved HbO₂ and Hb within the lumen of the SV (Figures 1D, 2A, and 3A) before and after activation (Figures 3G and 3H) and calculated the SO₂ and TBV, respectively (Figures 3I and 3J). We observed that SO₂ dropped significantly after NE activation in the SV from 70% ± 15% (NE-) to 55% ± 16% (NE+) ($p = 0.0008$; Figure 3I). The optoacoustic signals reporting TBV in SV increased significantly after activation from 0.14 ± 0.03 (NE-) to 0.20 ± 0.05 (NE+) ($p = 0.0002$; Figure 3J). No SO₂ or TBV changes were observed in the SV of control animals injected with saline (data not shown). In an artery used as reference (indicated with a white box in Figure 3A), neither the SO₂ nor the TBV increased significantly. These findings demonstrate that SO₂ and TBV gradients in BAT and in the SV can be resolved in mice and indicate metabolic activity. SO₂ gradients could be regarded as indicative of metabolic demand (oxygen utilization), whereas TBV changes indicate change in blood flow/perfusion of the area observed. This feature may lead to better quantification of relative activation changes in the study of metabolism *in vivo*.

To examine whether MSOT could record browning of WAT by β 3-adrenergic remodeling of WAT, female nude mice ($n = 3$) were injected over 10 consecutive days with CL316,243 (CL). *Ex vivo* MSOT measurements of ingWAT, browned ingWAT, and BAT revealed a distinct difference in optoacoustic signal intensity (Figure 4A) and in the optoacoustic spectra recorded (Figure 4B) between browned and control ingWAT (CL, 44 ± 6 a.u.; control, 25 ± 7 a.u.). *In vivo* measurements of the ingWAT region of CL-treated mice (Figure 4C) showed a decrease in SO₂ compared with control animals (CL, 66% ± 6%; control, 79% ± 8%; $p = 0.08$) (Figure 4D).

MSOT Handheld Measurements and Indirect Calorimetry in Human Subjects

The neck and the supraclavicular region of volunteers ($n = 3$) who displayed ¹⁸F-FDG uptake in BAT were imaged using video-rate handheld MSOT (Figure S1B), to interrogate whether BAT could be optoacoustically measured in humans (Figures 5A–5F). Oblique slices (Figures 5B and 5C) were extracted from volumetric PET images co-registered with MRI images (Figure 5A). MRI (Fig-

ure 5D) and co-registered MRI-PET slices (Figure 5E) of the supraclavicular region (i.e., the ROI outlined with a yellow dotted line on Figure 5C) were used to validate corresponding MSOT images (Figure 5F) obtained from the same region. Since PET resolution is ~9 mm, MRI oblique resolution is ~3 mm, and MSOT resolution is ~0.3 mm, the MSOT oblique-slice image (Figure 5F) gives a more detailed view of the tissue than oblique PET or oblique MRI. The MSOT image captures information corresponding to a triangular muscle structure, enclosed by the outer skin boundary and the dotted line in Figure 5F, which is also visible in the oblique MR image (Figure 5D), albeit with much lower resolution. On the anterior side of the muscle lies metabolically active adipose tissue (white arrow; Figure 5F), identified on the PET-MR images (Figures 5A, 5D, and 5E) as a BAT region.

In a next step, activation was induced via cold exposure of the whole body by means of a suit perfused with 13°C cold water ($n = 3$). IC measurements of oxygen consumption were conducted in parallel to the MSOT measurements for validation purposes (Figure 5G), using an exercise physiology kit (ML3508B80 Exercise Physiology System, AD Instruments). MSOT images were obtained before and after cold exposure. BAT images (Figure 5H) obtained from the area marked with a white arrow in Figure 5F exhibited higher optoacoustic signal after activation compared with the areas from the muscle region indicated by the green arrow on Figure 5F (for more details, see Movie S1). Other vascular structures within BAT tissue and at the interface between BAT and the surrounding muscle regions also exhibited post-activation signal changes (Figures S4C and S4D).

Similar to the animal measurements, the HbO₂ signal intensity from BAT correlated with the corresponding $\dot{V}O_2$ measurements (Figure 5I). The HbO₂ intensity in the BAT region changed significantly with cold activation (0.34 ± 0.12 at baseline versus 0.92 ± 0.08 after cooling, $p = 0.004$), whereas no significant activity was captured from the muscle region (0.29 ± 0.09 at baseline and 0.37 ± 0.08 after cooling, $p = 0.09$). Small signal variations were observed in the skin (0.98 ± 0.04 at baseline and 1.16 ± 0.04 after cooling, $p = 0.05$) (Figure 5J). In contrast to muscle and BAT, which are illuminated with diffusive light, the skin receives concentrated light energy. Therefore such changes could be at least partially explained as small thermal effects, in analogy to the animal measurements. The percentage change in three individuals showed that the optoacoustic signal in the muscle changes 1% ± 2%, whereby the $\dot{V}O_2$ changes 4.5% ± 1% and the optoacoustic signal in the BAT changes 372% ± 105% (Figure 5K). This is in accordance with the findings of SO₂ and TBV, which show a clear increase in BAT, but not in muscle, after cooling (Figures S4A and S4B). Thus, the results demonstrate that MSOT can optoacoustically detect BAT and activation in humans.

Hemoglobin, Fat, and Water MSOT of BAT and WAT in Human Volunteers

In a final step, we examined the imaging features of human BAT versus WAT provided by MSOT. Optoacoustic imaging was performed by illuminating the supraclavicular region of ten volunteers in the 700–970 nm spectral region, and in this case four tissue components were unmixed, i.e., fat and water in addition to Hb and HbO₂. All measurements were performed by a trained

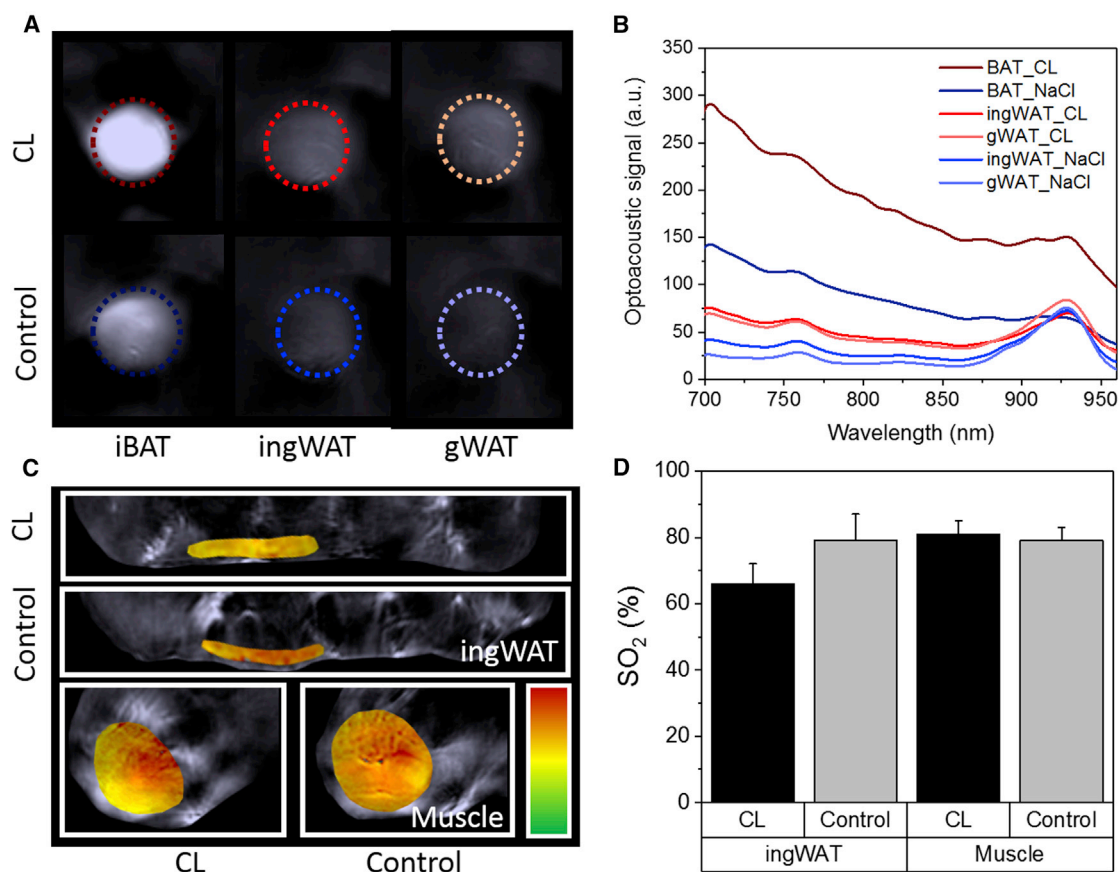


Figure 4. Ex Vivo and In Vivo Comparison of the Optoacoustic Signal Generated from Brown, Beige, and White Adipose Tissue

(A) Reconstructed optoacoustic images of excised iBAT, ingWAT, and gWAT from animals treated with CL316,243 (CL) and control animals measured at 800 nm in a scattering phantom.

(B) Optoacoustic spectra of *ex vivo* iBAT, ingWAT, and gWAT of animals treated with CL and control animals in the NIR as measured by MSOT.

(C) Reconstructed anatomical MSOT images at 800 nm (gray scale) with overlay blood oxygen saturation (SO₂) map (green-red scale) in ingWAT and muscle region for CL-treated and control animals.

(D) Normalized signal of SO₂ in ingWAT and muscle of CL-treated and control animals. Data are represented as mean ± SEM.

physician who was guided by MSOT-present anatomical features to reliably identify the same anatomical region in the volunteers scanned. Reproducibility studies performed by removing and placing the MSOT head back onto the supraclavicular lesion of one individual demonstrated our ability to reliably identify the same anatomical features, yielding virtually identical MSOT spectra (Figures 6A–6C). All volunteers were also imaged by a multi-echo gradient-echo MRI sequence in a 3 T clinical scanner (see STAR Methods for details).

Spectrally, fat and water absorb primarily in the 900–950 nm spectral region, whereby hemoglobins absorb primarily in the 700–900 nm spectral window. To examine whether MSOT could distinguish BAT and WAT at rest, we unmixed images for fat and TBV from the MSOT images collected from human volunteers (see STAR Methods for details). We then plotted a distribution chart depicting the content of fat and TBV of each pixel (Figure 6D) that was found within the lipid-rich areas of the unmixed fat image (Figure 6E). The plotted distribution demonstrated different populations of pixels, in terms of fat and TBV content. By color coding pixels belonging to different

clusters of the fat-TBV chart (Figure 6D), it was possible to identify BAT from WAT distributions within the lipid-rich area of the MSOT image. To further validate the result of clustering, we plotted the spectra measured from the BAT regions, which exhibited a characteristically different spectral pattern and four times stronger optoacoustic signal in the 700–900 nm window compared with spectra obtained from WAT regions (Figure 6F). Both BAT and WAT spectra show strong signals at ~930 nm, representative of absorption by fat/lipids. In contrast, a spectrum collected from muscle shows strong hemoglobin signals but absence of a strong fat peak (Figure 6G), further confirming the MSOT ability to spectrally distinguish tissue composition.

Transverse tomographic MRI and MRI proton density fat fraction (PDFF) maps were obtained from the shoulder region of the volunteers (Figures S5A–S5D). Low MRI-PDFF values indicate the presence of BAT, whereas high MRI-PDFF values indicate WAT. Water/fat MSOT images revealed a layered structure consistent with skin, subcutaneous fat, and deeper-seated muscle and fat tissues. An MSOT fat fraction (FF) and

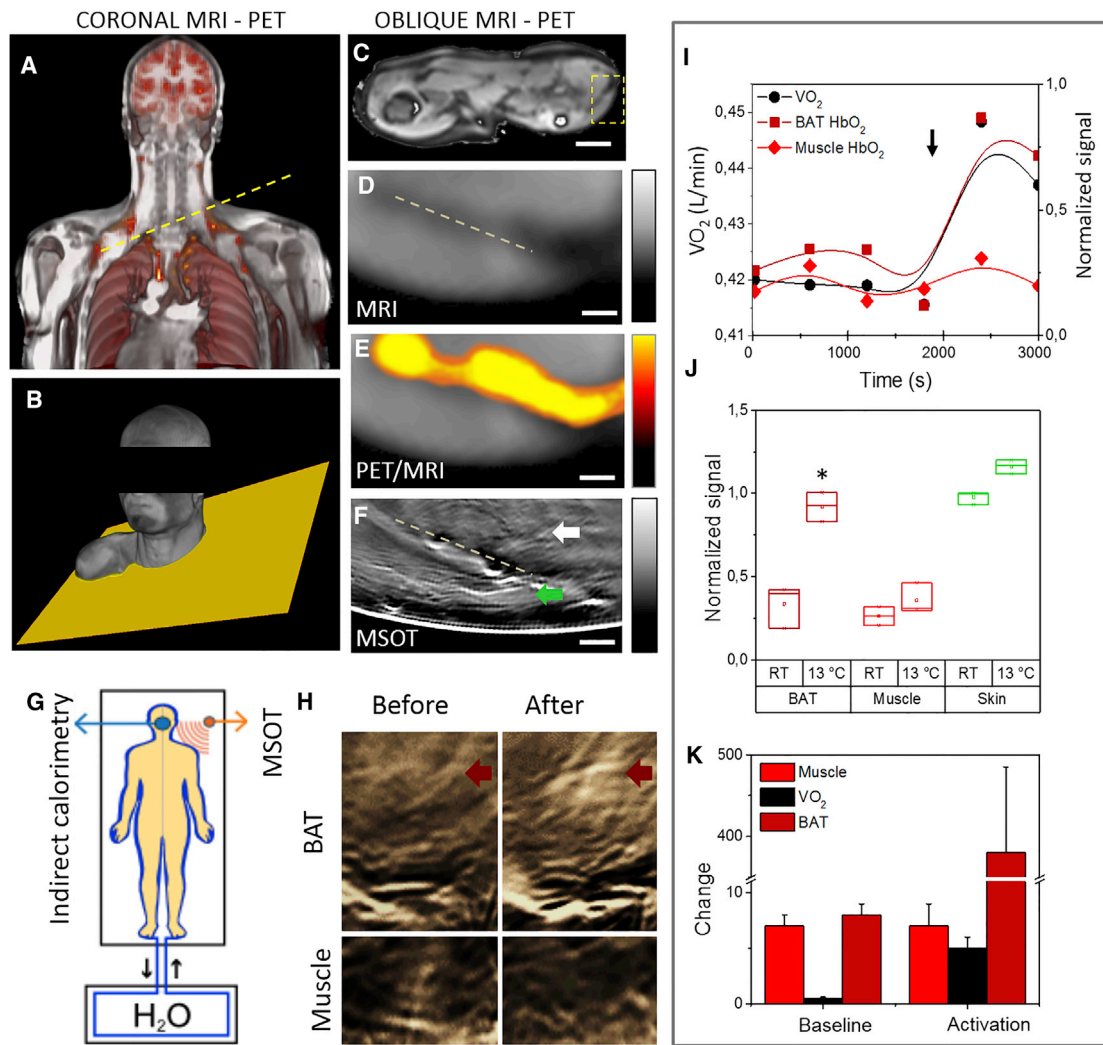


Figure 5. Handheld MSOT of Human Volunteers

(A) MRI-PET coronal co-registration of the upper torso of a volunteer; the MSOT imaging plane is indicated by the yellow dotted line. (B) Three-dimensional MRI rendering of (A), with the MSOT imaging angle indicated as a yellow plane. (C) Oblique MRI slice of the shoulder region along the yellow plane in (B). (D) MR image of the supraclavicular region shown in (C) as a dotted-line box. (E) Registration of the corresponding PET signal (color) on (D), showing ^{18}F -FDG uptake in activated BAT. (F) MSOT handheld image from the same region as in (D), showing BAT (white arrow) and muscle (green arrow). (G) Schematic of simultaneous indirect calorimetry and MSOT measurements of cold activation using 13°C water. (H) Before and after cold activation, MSOT was used to image BAT (red arrows) and muscle areas indicated on (F) with white and green arrows, respectively. (I) HbO_2 signals from BAT and muscle, and corresponding $\dot{V}\text{O}_2$ measurements over the time recorded. The black arrow indicates the beginning of cold exposure. (J) Relative changes of signal intensity in BAT, muscle, and skin before and 10 min after cold exposure. RT, room temperature. (K) Comparative percentage change between baseline (baseline 0–1,800 s) and baseline plus activation (activation 0–3,000 s) in muscle, $\dot{V}\text{O}_2$, and BAT ROIs ($n = 3$). Scale bars, 5 cm (C), 5 mm (D–F). * $p < 0.05$. Data are represented as mean \pm SEM.

an MSOT TBV fat fraction (BFF) were computed (Figure S5) from the area expected to contain BAT and WAT, in analogy to the MRI-PDFF. MSOT-FF and changes observed from the BAT/WAT area in different volunteers (Figures S5F and S5I) corresponded to changes in vascularization and water content between BAT and WAT (Figures S5G and S5J). Areas of low MSOT-FF were accompanied by a corresponding increase in vascular volume, consistent with the presence of BAT. Conversely, volunteers with high MSOT-FF and low Hb/HbO_2

signals indicated relative absence of BAT, in favor of WAT. Even if MSOT and MR images were not accurately co-registered in the study, but only approximately obtained from the same volume, we correlated MSOT-FF to MRI-PDFF values and found a positive correlation showing a Spearman correlation coefficient of 0.55 ($p = 0.04$) (Figure S5K). The correlation between MSOT-BFF and MRI-PDFF shows a negative correlation with a Spearman correlation coefficient of -0.69 ($p = 0.02$) (Figure S5L).

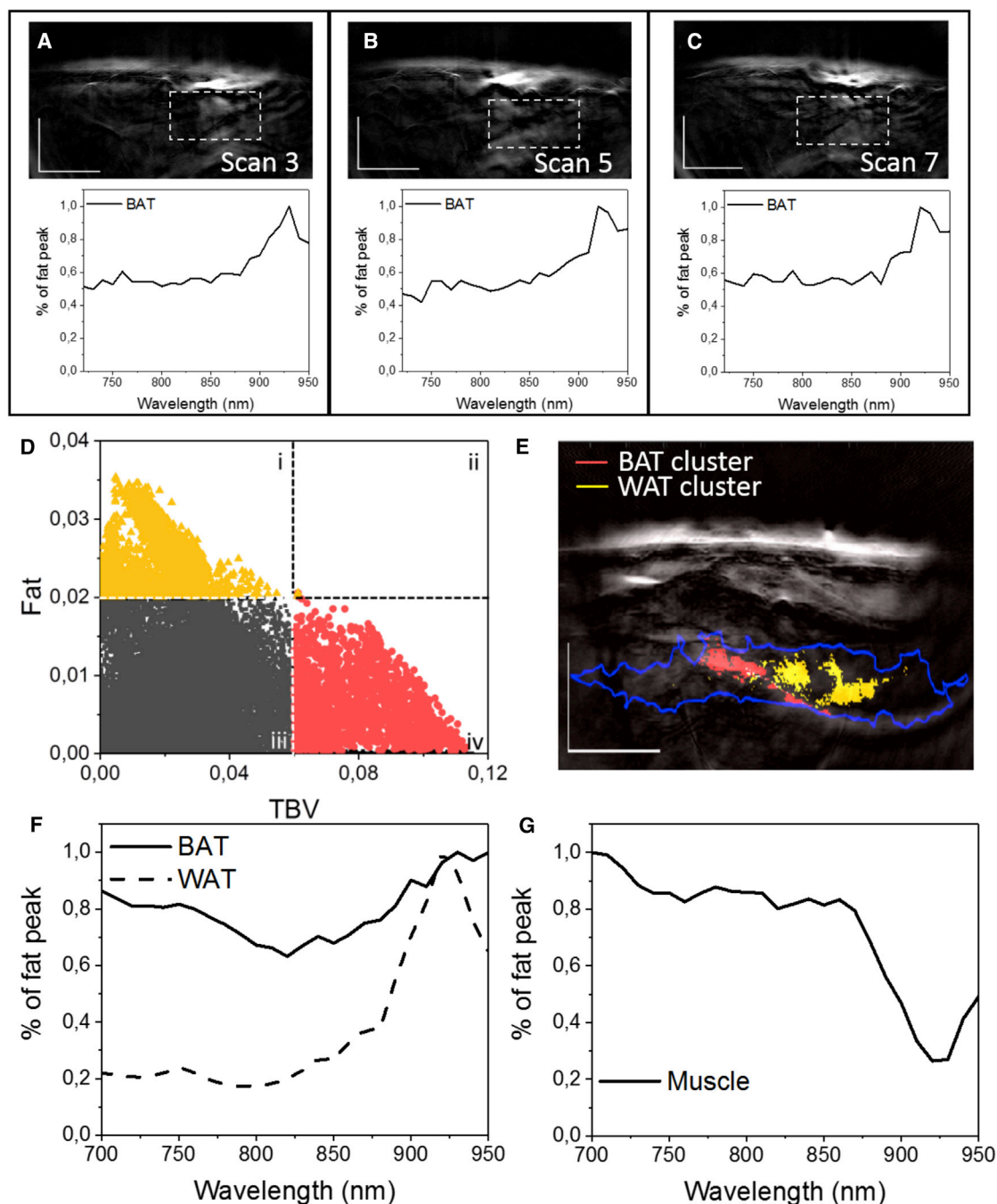


Figure 6. Handheld Multi-spectral Optoacoustic Tomography Imaging of the Human Supraclavicular Region at Rest

(A–C) Individual MSOT scans of right supraclavicular region in a volunteer with confirmed brown adipose tissue (BAT) by magnetic resonance proton density fat fraction and the corresponding BAT spectra measured at the expected depths of the supraclavicular BAT depot. (A) Scan 3, (B) scan 5, and (C) scan 7.

(D) Scatterplot of fat and total blood volume intensities of pixels at the expected depths of BAT in the supraclavicular region. Shown are pixels with high fat and lower blood content (yellow pixels), pixels with lower fat content but higher blood content (red pixels), and pixels that belong to neither of the two classes (dark gray pixels).

(E) Spatial localization of the two classes from (D) in the anatomic image at 800 nm (gray scale); they form two clusters at the expected depths of supraclavicular BAT (encircled by the blue line): one cluster contains pixels with higher fat intensity (yellow) and the other pixels with higher blood intensity (red).

(F) Mean spectral profile of the two clusters where the WAT curve represents the mean spectrum of the yellow cluster in (E) and the BAT curve represents the mean spectrum of the red cluster in (E).

(G) Spectrum of manually defined skeletal muscle region.

Scale bars, 1 cm.

DISCUSSION

In addition to its thermoregulatory function, BAT is implicated in energy homeostasis due to its ability to combust high amounts of nutrient energy (Himms-Hagen, 1979; Rothwell and Stock, 1979). In humans, a negative correlation between BAT activity after cold exposure and BMI and fat mass was demonstrated (Saito et al., 2009; van Marken Lichtenbelt et al., 2009). These observations have directed investigations that aim to alter BAT mass and activity to counteract energy imbalance (Vijgen and van Marken Lichtenbelt, 2013). In such studies, quantitative measurements of BAT metabolism can radically complement generic weight gain or loss or body composition measurements by providing observations of the effects of substances, drugs, and environmental factors on metabolism *in vivo*.

Overall, the development of label-free non-ionizing radiation methods for non-invasive quantitative measurement of energy expenditure can change the landscape of studying metabolism in BAT and other tissues *in vivo*. A critical step toward this direction is achieved by the development of handheld MSOT (Buehler et al., 2013; Taruttis and Ntziachristos, 2015), which yielded herein accurate spectral measurements of metabolic readings. Even though hemoglobin has long been recognized as a source of contrast for NIR spectroscopy and diffuse optical tomography (Ntziachristos et al., 2005), the poor resolution of these techniques has limited the accuracy and the range of reliable applications (Ntziachristos, 2010). Hemoglobin is also employed in optoacoustic (photoacoustic) imaging to visualize blood vessels and microvasculature (Karlas et al., 2017; Taruttis and Ntziachristos, 2015). Conversely, by applying *macroscopic* optoacoustic imaging in the NIR, we resolved not only vasculature but also general tissue features and related, for the first time, high-resolution tissue hemoglobin readings in metabolic measurements of brown fat, confirmed by IC. Imaging of tissue HbO₂ and Hb was achieved by employing key technology advances. First, curved detector arrays significantly improved image quality over linear arrays clinically applied in the past and allowed morphological imaging of tissue structures in mice and humans. Second, we employed detectors custom-designed for optoacoustic imaging, which allowed broader frequency-band detection over conventional ultrasound arrays, typically manufactured for operation in narrow bandwidths. Third, the acquisition of one cross-sectional frame per laser pulse and wavelength, based on a new class of fast-switch lasers, and advanced image-reconstruction models enabled motion-free accurate image reconstructions and, importantly, allowed the seamless use of an extended spectral range (700–950 nm) within scan times lasting seconds, which yielded simultaneous reconstructions of Hb, HbO₂, lipid, and water tissue content.

Capitalizing on the above-mentioned advances in imaging performance, MSOT resolved BAT activation in mice and humans. MSOT separated HbO₂ and Hb in high resolution, computed SO₂ and TBV values, and further unmixed fat and water based on a non-invasive, handheld modality, which operates with non-ionizing radiation and in label-free mode. Compared with ¹⁸F-FDG-PET, the current gold standard for imaging metabolic activity, MSOT is shown to open new possibilities for BAT and possibly other tissue metabolism measurements by allowing label-free, handheld (portable), longitudinal, and disseminated

operation, without the need to use radio-isotopes. These features are not offered by any other radiological method today.

Oxygen consumption is an indirect but definitive measure of aerobic metabolism, supported by an increase in blood flow reflecting greater oxygen demand (Foster and Frydman, 1979; Puchalski et al., 1987). SO₂ and TBV values of activated BAT strongly correlated with IC measurements in mice and IC and PET in humans, showing timing differences compared with the corresponding HbO₂ and Hb signals. To assess dynamic tissue responses, we also computed SO₂ and TBV rates (time gradients). While the SO₂ value statically reveals the tissue oxygenation state at a given time point, the SO₂ rate is proposed as a more precise marker of oxygen consumption. Likewise, the TBV rate is proposed as a measure of blood volume influx (tissue perfusion). BAT activation was manifested by a corresponding increase in SO₂ rate (Figure 3E) and an initially positive blood flow rate (BAT perfusion; Figure 3F), which subsequently becomes negative when tissue oxygen demand is met. In the future, a higher sampling rate may allow a more precise determination of SO₂ and TBV rates, possibly revealing a more detailed picture of the temporal evolution of BAT activation.

IC was employed herein as the gold standard for the analysis of energy expenditure in rodents (Cannon and Nedergaard, 2011; Even and Nadkarni, 2012; Tschop et al., 2012), and was also considered for the validation of human measurements based on correlative $\dot{V}O_2$ monitoring. Computed TBV and SO₂ values exhibited a 4-fold stronger local SO₂ change in brown fat over a global $\dot{V}O_2$ value, also recorded as a SO₂ change in the SV (Figure S3G). This finding indicates that MSOT may provide a more accurate measurement of metabolism than IC, since the optoacoustic method measures tissue responses in a localized fashion, whereas IC records activity in a delayed and global fashion.

In addition to recording activation and metabolic changes, MSOT was also shown to be capable of identifying imaging features associated with BAT morphology. BAT showed a substantially different spectrum from WAT, possibly explained by the higher content of mitochondria, leading to the characteristic darker brownish color, in contrast to the lighter white or yellow appearance of WAT (Enerback, 2009). While these differences are expected within the visible spectrum, we showed that spectral differences also exist in the NIR. Furthermore, BAT exhibited a 2-fold higher overall intensity than WAT (Figure 1), possibly due to a combination of the different spectral profiles and the profuse BAT vascularization over WAT in mice.

Conversely, the iBAT region of diabetic mice exhibited a weaker intensity (~20% decrease) compared with healthy controls (Figure S3). Moreover, β_3 -adrenergic remodeling of WAT and thereby induction of browning led to an increase in signal intensity of ingWAT and gWAT (~50% increase) compared with WAT, but a decrease in SO₂ signal due to increased metabolic activity (Figure 4). In contrast to ¹⁸F-FDG-PET studies, the localization of brown fat is achieved without the need for contrast agents or cold activation (Wu et al., 2014). Moreover, spectral interrogation at the 900–970 nm window enabled unmixing of fat and water contributions, which offered a previously undisclosed look into MSOT imaging features in terms of water and fat composition in subcutaneous and BAT/WAT-related lipid content. Reduced lipid content in the BAT area was congruent with increased vascularization seen on the 700–900 nm MSOT

images and consistent with BAT anatomy and physiology. Different MSOT metrics (SO_2 , TBV, HbO_2 , Hb, fat, or water) could be contrasted with MRI measurements. In a pilot investigation we derived the MSOT-FF and MSOT-BFF measured in the supraclavicular region and demonstrated a statistically significant correlation between MSOT-FF, MSOT-BFF, and MRI-PDFF (Figure S5). This correlation is striking given that the MSOT and MR images are not rigorously co-registered but only approximately obtained from the same tissue area. In addition, we compared the spectral information of BAT, WAT at the depth of the BAT depot, and muscle of the supraclavicular region. BAT showed marked spectral differences and increased signal intensity in the blood region of the spectra (700–900 nm) compared with WAT (Figure 6F), which is similar to the observations in mice (Figure 1). The handheld MSOT system employed achieves penetration depths of ~2–3 cm. The penetration depth depends on the wavelength employed, the particular optical properties of the tissue scanned, and the amount of energy per illumination pulse. During our scans we illuminated tissue with pulse energy of less than 15 mJ at a repetition range of 25 Hz. Higher pulse energies and illumination schemes are allowed from a regulatory standpoint and would enable imaging at higher penetration depths up to ~4 cm, while complying with the maximum energy values for human applications (~20 mJ/cm²). Considering that the thickness of WAT ranges ~3–3.5 cm over different BAT depots such as the retroperitoneal depot, it may be possible in the future to image this ROI as well (Diot et al., 2017).

To demonstrate the intra-user reproducibility of our handheld MSOT system we measured a volunteer with confirmed BAT (by MRI-PDFF) 10 times in each supraclavicular region (right and left side), resulting in an MSOT-FF value of 0.67 with a low standard error of the mean (SEM = 0.03), i.e., a small variability, similar to findings of handheld ultrasonography studies (Massagli et al., 1989).

Even though BAT metabolism was a primary focus herein, MSOT may be more generally applied to a larger range of applications spanning exercise physiology, bioenergetic/obesity-related studies, and different metabolic diseases such as metabolic syndrome, mitochondrial diseases, and disorders of lipid metabolism. By enabling longitudinal and point-of-care measurements, or even possibly measurements based on wearable sensors, the method could support scientific research well beyond the limitations set by the complexity of radio-isotope production, the short lifetimes of radio-isotopes, and the frequency of the measurement performed. Nevertheless, *in vivo* MSOT is limited to 2–3 cm penetration depth; therefore, we anticipate its use primarily in small animals and specific human interrogations. The safe use of and ability to expand routine MSOT use to outpatient care may enable the study of metabolism in a personalized manner.

Study Limitations

The study showcases MSOT as an imaging technology that can visualize BAT and analyze spectral features that differentiate it from WAT *in vivo* in mice and humans. MSOT also demonstrated the ability to visualize BAT activation, based on hemoglobin gradients, and correlated these measurements to IC recordings. Nevertheless, this first application and demonstration of MSOT imaging of tissue metabolism and BAT/WAT hemoglobin, lipid,

and water composition needs to be corroborated by follow-up studies that will address current limitations, i.e.:

- Standardize an MSOT and MRI study protocol that allows better image co-registration and therefore allows a more precise comparison between water and lipid signals between the two methods, as well as the added value of the hemoglobin signal in the study of tissue metabolism, beyond BAT and WAT.
- Possibly perform a larger cohort study comparing ¹⁸F-FDG-PET imaging with MSOT. PET remains the gold standard for imaging activated BAT in humans, but its use of radioactivity makes it impractical for longitudinal and disseminated studies. Therefore, it would be of great interest to investigate the correlation between ¹⁸F-FDG uptake and MSOT oxygen consumption and blood volume/flow studies to identify whether MSOT could support PET studies in tissue metabolism protocols and provide a larger number of observations over extended periods of time.
- In analogy to conventional ultrasonography, clinical handheld MSOT allows fast (video-rate) cross-sectional tissue visualization but is not well suited to measuring the total BAT mass and energy expenditure as may be provided by a full-body imaging system. Moreover, the penetration depth afforded by MSOT (~2–5 cm depending on tissue type) limits access to deep-seated tissues. The achieved penetration depth is a hard limitation for MSOT and should be taken into account when considering MSOT studies of tissue metabolism.

STAR★METHODS

Detailed methods are provided in the online version of this paper and include the following:

- KEY RESOURCES TABLE
- CONTACT FOR REAGENT AND RESOURCE SHARING
- EXPERIMENTAL MODEL AND SUBJECT DETAILS
 - Animals
 - Humans
- METHOD DETAILS
 - Animals
 - Multi-spectral Optoacoustic Tomography
 - Indirect Calorimetry
 - Mouse MSOT Measurements Ex Vivo
 - Mouse MSOT Measurements In Vivo
 - Cryoslicing
 - Model-Based Reconstruction and Data Analysis
 - MSOT Handheld Measurements and Indirect Calorimetry in Human Subjects
 - MRI –MSOT Correlation in Human Subjects
- QUANTIFICATION AND STATISTICAL ANALYSIS
- DATA AND SOFTWARE AVAILABILITY

SUPPLEMENTAL INFORMATION

Supplemental Information includes five figures, one table, and one movie and can be found with this article online at <https://doi.org/10.1016/j.cmet.2018.02.002>.

ACKNOWLEDGMENTS

The authors would like to thank Uwe Klemm and Sarah Glasl for technical support. The research leading to these results has received funding from the Deutsche Forschungsgemeinschaft (DFG), Sonderforschungsbereich 824 (SFB-824), subproject A1, and KL 973/11-1. We furthermore acknowledge funding from the European Research Council under the European Union's Seventh Framework Programme (FP/2007-2013)/ERC Grant Agreement No. 233161 (MSOT) Next Generation *in vivo* imaging platform for post-genome biology and medicine MSOT and funding from EU FP7 Project DIABAT (HEALTH-F2-2011-278373). D.C.K. acknowledges an ERC Starting Grant (grant agreement no. 677661, ProFatMRI). This work was additionally supported by the Helmholtz cross-program topic "Metabolic Dysfunction."

AUTHOR CONTRIBUTIONS

J.R., M.W., and A.K. conceived the idea, designed and performed the experiments, analyzed and interpreted the data, and wrote the manuscript. K.P.-Y. analyzed data and provided intellectual input. G.D. performed experiments and analyzed data. D.F. and D.C.K. conducted experiments and provided intellectual input. T.F., S.V.O., N.B., E.D., C.H., and H.H. provided intellectual input. M.K. and V.N. conceived the idea, designed and guided the studies, provided intellectual input, and wrote the manuscript.

DECLARATION OF INTERESTS

V.N. holds ownership interest (including patents) in iThera Medical. No potential conflicts of interest were disclosed by the other authors.

Received: May 18, 2017

Revised: November 22, 2017

Accepted: February 5, 2018

Published: March 6, 2018

REFERENCES

- Abreu-Vieira, G., Hagberg, C.E., Spalding, K.L., Cannon, B., and Nedergaard, J. (2015). Adrenergically stimulated blood flow in brown adipose tissue is not dependent on thermogenesis. *Am. J. Physiol. Endocrinol. Metab.* *308*, E822–E829.
- Baum, T., Cordes, C., Dieckmeyer, M., Ruschke, S., Franz, D., Hauner, H., Kirschke, J.S., and Karampinos, D.C. (2016). MR-based assessment of body fat distribution and characteristics. *Eur. J. Radiol.* *85*, 1512–1518.
- Bauwens, M., Wierts, R., van Royen, B., Bucerius, J., Backes, W., Mottaghy, F., and Brans, B. (2014). Molecular imaging of brown adipose tissue in health and disease. *Eur. J. Nucl. Med. Mol. Imaging* *41*, 776–791.
- Buehler, A., Kacprowicz, M., Taruttis, A., and Ntziachristos, V. (2013). Real-time handheld multispectral optoacoustic imaging. *Opt. Lett.* *38*, 1404–1406.
- Cannon, B., and Nedergaard, J. (2004). Brown adipose tissue: function and physiological significance. *Physiol. Rev.* *84*, 277–359.
- Cannon, B., and Nedergaard, J. (2011). Nonshivering thermogenesis and its adequate measurement in metabolic studies. *J. Exp. Biol.* *214*, 242–253.
- Chen, Y.I., Cypess, A.M., Sass, C.A., Brownell, A.L., Jokivarsi, K.T., Kahn, C.R., and Kwong, K.K. (2012). Anatomical and functional assessment of brown adipose tissue by magnetic resonance imaging. *Obesity (Silver Spring)* *20*, 1519–1526.
- Crane, J.D., Mottillo, E.P., Farncombe, T.H., Morrison, K.M., and Steinberg, G.R. (2014). A standardized infrared imaging technique that specifically detects UCP1-mediated thermogenesis *in vivo*. *Mol. Metab.* *3*, 490–494.
- Dicker, A., Cannon, B., and Nedergaard, J. (1995). Cold acclimation-recruited nonshivering thermogenesis: the Syrian hamster is not an exception. *Am. J. Physiol.* *269*, R767–R774.
- Dima, A., Burton, N.C., and Ntziachristos, V. (2014). Multispectral optoacoustic tomography at 64, 128, and 256 channels. *J. Biomed. Opt.* *19*, 36021.
- Diot, G., Dima, A., and Ntziachristos, V. (2015). Multispectral opto-acoustic tomography of exercised muscle oxygenation. *Opt. Lett.* *40*, 1496–1499.
- Diot, G., Metz, S., Noske, A., Liapis, E., Schroeder, B., Ovsepian, S.V., Meier, R., Rummeny, E., and Ntziachristos, V. (2017). Multispectral optoacoustic tomography (MSOT) of human breast cancer. *Clin. Cancer Res.* *23*, 6912–6922.
- Enerback, S. (2009). The origins of brown adipose tissue. *N. Engl. J. Med.* *360*, 2021–2023.
- Even, P.C., and Nadkarni, N.A. (2012). Indirect calorimetry in laboratory mice and rats: principles, practical considerations, interpretation and perspectives. *Am. J. Physiol. Regul. Integr. Comp. Physiol.* *303*, R459–R476.
- Foster, D.O., and Frydman, M.L. (1978). Nonshivering thermogenesis in the rat. II. Measurements of blood flow with microspheres point to brown adipose tissue as the dominant site of the calorogenesis induced by noradrenaline. *Can. J. Physiol. Pharmacol.* *56*, 110–122.
- Foster, D.O., and Frydman, M.L. (1979). Tissue distribution of cold-induced thermogenesis in conscious warm- or cold-acclimated rats reevaluated from changes in tissue blood flow: the dominant role of brown adipose tissue in the replacement of shivering by nonshivering thermogenesis. *Can. J. Physiol. Pharmacol.* *57*, 257–270.
- Golozoubova, V., Cannon, B., and Nedergaard, J. (2006). UCP1 is essential for adaptive adrenergic nonshivering thermogenesis. *Am. J. Physiol. Endocrinol. Metab.* *291*, E350–E357.
- Golozoubova, V., Hohtola, E., Matthias, A., Jacobsson, A., Cannon, B., and Nedergaard, J. (2001). Only UCP1 can mediate adaptive nonshivering thermogenesis in the cold. *FASEB J.* *15*, 2048–2050.
- Granneman, J.G., Burnazi, M., Zhu, Z., and Schwamb, L.A. (2003). White adipose tissue contributes to UCP1-independent thermogenesis. *Am. J. Physiol. Endocrinol. Metab.* *285*, E1230–E1236.
- Heldmaier, G., and Ruf, T. (1992). Body temperature and metabolic rate during natural hypothermia in endotherms. *J. Comp. Physiol. B* *162*, 696–706.
- Himms-Hagen, J. (1979). Obesity may be due to a malfunctioning of brown fat. *Can. Med. Assoc. J.* *121*, 1361–1364.
- Hu, H.H., and Kan, H.E. (2013). Quantitative proton MR techniques for measuring fat. *NMR Biomed.* *26*, 1609–1629.
- Karampinos, D.C., Melkus, G., Baum, T., Bauer, J.S., Rummeny, E.J., and Krug, R. (2014). Bone marrow fat quantification in the presence of trabecular bone: initial comparison between water-fat imaging and single-voxel MRS. *Magn. Reson. Med.* *71*, 1158–1165.
- Karampinos, D.C., Yu, H., Shimakawa, A., Link, T.M., and Majumdar, S. (2011). T(1)-corrected fat quantification using chemical shift-based water/fat separation: application to skeletal muscle. *Magn. Reson. Med.* *66*, 1312–1326.
- Karlas, A., Reber, J., Diot, G., Bozhko, D., Anastasopoulou, M., Ibrahim, T., Schwaiger, M., Hyafil, F., and Ntziachristos, V. (2017). Flow-mediated dilatation test using optoacoustic imaging: a proof-of-concept. *Biomed. Opt. Express* *8*, 3395–3403.
- Klingenspor, M. (2003). Cold-induced recruitment of brown adipose tissue thermogenesis. *Exp. Physiol.* *88*, 141–148.
- Massagli, T.L., Cardenas, D.D., and Kelly, E.W. (1989). Experience with portable ultrasound equipment and measurement of urine volumes: inter-user reliability and factors of patient position. *J. Urol.* *142*, 969–971.
- Meyer, C.W., Willershauser, M., Jastroch, M., Rourke, B.C., Fromme, T., Oelkrug, R., Heldmaier, G., and Klingenspor, M. (2010). Adaptive thermogenesis and thermal conductance in wild-type and UCP1-KO mice. *Am. J. Physiol. Regul. Integr. Comp. Physiol.* *299*, R1396–R1406.
- Mirbolooki, M.R., Constantinescu, C.C., Pan, M.L., and Mukherjee, J. (2011). Quantitative assessment of brown adipose tissue metabolic activity and volume using 18F-FDG PET/CT and β 3-adrenergic receptor activation. *EJNMMI Res.* *1*, 30.
- Nakayama, A., Bianco, A.C., Zhang, C.Y., Lowell, B.B., and Frangioni, J.V. (2003). Quantitation of brown adipose tissue perfusion in transgenic mice using near-infrared fluorescence imaging. *Mol. Imaging* *2*, 37–49.

- Nedergaard, J., Bengtsson, T., and Cannon, B. (2007). Unexpected evidence for active brown adipose tissue in adult humans. *Am. J. Physiol. Endocrinol. Metab.* *293*, E444–E452.
- Nicholls, D.G., and Locke, R.M. (1984). Thermogenic mechanisms in brown fat. *Physiol. Rev.* *64*, 1–64.
- Nnodim, J.O., and Lever, J.D. (1988). Neural and vascular provisions of rat interscapular brown adipose tissue. *Am. J. Anat.* *182*, 283–293.
- Ntziachristos, V. (2010). Going deeper than microscopy: the optical imaging frontier in biology. *Nat. Methods* *7*, 603–614.
- Ntziachristos, V., Ripoll, J., Wang, L.V., and Weissleder, R. (2005). Looking and listening to light: the evolution of whole-body photonic imaging. *Nat. Biotechnol.* *23*, 313–320.
- Ohlson, K.B., Lindahl, S.G., Cannon, B., and Nedergaard, J. (2003). Thermogenesis inhibition in brown adipocytes is a specific property of volatile anesthetics. *Anesthesiology* *98*, 437–448.
- Ohlson, K.B., Mohell, N., Cannon, B., Lindahl, S.G., and Nedergaard, J. (1994). Thermogenesis in brown adipocytes is inhibited by volatile anesthetic agents. A factor contributing to hypothermia in infants? *Anesthesiology* *81*, 176–183.
- Ouellet, V., Labbé, S.M., Blondin, D.P., Phoenix, S., Guérin, B., Haman, F., Turcotte, E.E., Richard, D., and Carpentier, A.C. (2012). Brown adipose tissue oxidative metabolism contributes to energy expenditure during acute cold exposure in humans. *J. Clin. Invest.* *122*, 545–552.
- Puchalski, W., Bockler, H., Heldmaier, G., and Langefeld, M. (1987). Organ blood flow and brown adipose tissue oxygen consumption during noradrenaline-induced nonshivering thermogenesis in the Djungarian hamster. *J. Exp. Zool.* *242*, 263–271.
- Razansky, D., Buehler, A., and Ntziachristos, V. (2011). Volumetric real-time multispectral optoacoustic tomography of biomarkers. *Nat. Protoc.* *6*, 1121–1129.
- Rosenthal, A., Razansky, D., and Ntziachristos, V. (2010). Fast semi-analytical model-based acoustic inversion for quantitative optoacoustic tomography. *IEEE Trans. Med. Imaging* *29*, 1275–1285.
- Rothwell, N.J., and Stock, M.J. (1979). A role for brown adipose tissue in diet-induced thermogenesis. *Nature* *281*, 31–35.
- Saito, M., Okamatsu-Ogura, Y., Matsushita, M., Watanabe, K., Yoneshiro, T., Nio-Kobayashi, J., Iwanaga, T., Miyagawa, M., Kameya, T., Nakada, K., et al. (2009). High incidence of metabolically active brown adipose tissue in healthy adult humans: effects of cold exposure and adiposity. *Diabetes* *58*, 1526–1531.
- Smith, R.E., and Roberts, J.C. (1964). Thermogenesis of brown adipose tissue in cold-acclimated rats. *Am. J. Physiol.* *206*, 143–148.
- Taruttis, A., and Ntziachristos, V. (2015). Advances in real-time multispectral optoacoustic imaging and its applications. *Nat. Photon.* *9*, 219–227.
- Tschop, M.H., Speakman, J.R., Arch, J.R., Auwerx, J., Bruning, J.C., Chan, L., Eckel, R.H., Farese, R.V., Jr., Galgani, J.E., Hambly, C., et al. (2012). A guide to analysis of mouse energy metabolism. *Nat. Methods* *9*, 57–63.
- Tzoumas, S., Zaremba, A., Klemm, U., Nunes, A., Schaefer, K., and Ntziachristos, V. (2014). Immune cell imaging using multi-spectral optoacoustic tomography. *Opt. Lett.* *39*, 3523–3526.
- van Marken Lichtenbelt, W.D., Vanhomerig, J.W., Smulders, N.M., Drossaerts, J.M., Kemerink, G.J., Bouvy, N.D., Schrauwen, P., and Teule, G.J. (2009). Cold-activated brown adipose tissue in healthy men. *N. Engl. J. Med.* *360*, 1500–1508.
- Vijgen, G., and van Marken Lichtenbelt, W. (2013). Brown adipose tissue: clinical impact of a re-discovered thermogenic organ. *Front. Biosci.* *5*, 823–833.
- Vonnemann, J., Beziere, N., Bottcher, C., Riese, S.B., Kuehne, C., Dervede, J., Licha, K., von Schacky, C., Kosanke, Y., Kimm, M., et al. (2014). Polyglycerolsulfate functionalized gold nanorods as optoacoustic signal nanoamplifiers for in vivo bioimaging of rheumatoid arthritis. *Theranostics* *4*, 629–641.
- Wu, C., Cheng, W., Sun, Y., Dang, Y., Gong, F., Zhu, H., Li, N., Li, F., and Zhu, Z. (2014). Activating brown adipose tissue for weight loss and lowering of blood glucose levels: a microPET study using obese and diabetic model mice. *PLoS One* *9*, e113742.

STAR★METHODS

KEY RESOURCES TABLE

REAGENT or RESOURCE	SOURCE	IDENTIFIER
Chemicals, Peptides, and Recombinant Proteins		
CL 316243 disodium salt	Tocris, Bioscience	Cat. No. 1499
Streptozocin	Sigma-Aldrich	CAS Number 18883-66-4
Norepinephrine	Sanofi	ARTERENOL, PZN 03870227
NaCl 0,9%	B.Braun	Ecolav PE Flasche 30
Experimental Models: Organisms/Strains		
Mouse: hsd:ATHYMIC Nude-Foxn1 tm	Envigo	N/A
Mouse: BALB/cOlaHsd	Envigo	N/A
Software and Algorithms		
MATLAB R2017b	MathWorks	https://www.mathworks.com/products/matlab.html
ExpeData Version 1.1.22	Sable Systems International	https://www.sablesys.com/products/promethion-line/promethion-software/
LabChart software Version v.7.2	LabChart software	https://www.adinstruments.com/support/software
Model-based tomographic reconstruction method	Rosenthal et al., 2010	N/A
Linear unmixing	Diot et al., 2017	N/A
Other		
Altromin TPF Standard Diäten	Altromin Spezialfutter GmbH & Co	Altromin 1314

CONTACT FOR REAGENT AND RESOURCE SHARING

Further information and requests for resources and reagents should be directed to the Lead Contact, Vasilis Ntziachristos (v.ntziachristos@tum.de).

EXPERIMENTAL MODEL AND SUBJECT DETAILS

Animals

The mouse *in vivo* experiments were approved by the government of Upper Bavaria (Az.: 55.2-1-54-2532-123-13). Female nude mice (10 - 12 weeks old Nude-1 Foxn1; Harlan Laboratories, Germany) and male BALB/c mice (6 - 8 weeks old; Harlan Laboratories, Germany) were kept at 24±1°C and fed with standard rodent diet (Altromin 1314, Altromin Spezialfutter GmbH & Co, Germany) with free access to water. They were kept on a 12:12-h light-dark cycle. Animals were randomly assigned to experimental groups.

Humans

The study was approved by the Ethics Commission for the Faculty of Medicine of the Technical University of Munich (TUM). All participants gave written informed consent upon detailed explanation of the study and MSOT technology, its purpose, potential risks and data handling. All participants agreed to the use of their data for research purposes and publication of data/images upon anonymization. Thirteen healthy adult volunteers (8 males, 5 females; mean age 32), were recruited prospectively for the MRI/MSOT studies and the cold activation studies (further details are provided in the [Method Details](#) section). For the PET studies, three patients were retrospectively recruited at the oncology department. All patients had documented presence of BAT by PET imaging conducted within the routine clinical management. Due to the confidentiality policy followed by the oncology department further information on patient demographics cannot be provided. Analysis of the influence of the sex and gender identity was not performed as no difference is expected. Volunteers were grouped based on presence or absence of BAT.

METHOD DETAILS

Animals

A conventional diabetes animal model was employed by administering streptozocin (Sigma, Germany) at 150 mg/kg body weight to three male BALB/c mice (6 - 8 weeks old; Harlan Laboratories, Germany) via i.p. injection after 4 – 6 hours fasting. Three male control BALB/c mice (10 - 12 weeks old Nude-1 Foxn1; Harlan Laboratories, Germany) were injected with saline (0.9% NaCl).

For the induction of browning, three female nude mice (10 - 12 weeks old Nude-1 Foxn1; Harlan Laboratories, Germany) were treated with a daily i.p. injection of 1 mg/kg CL316,243 (Tocris, Bioscience) over 10 consecutive days. Three female nude control mice (10 - 12 weeks old Nude-1 Foxn1; Harlan Laboratories, Germany) were injected with saline (0.9% NaCl). All MSOT imaging experiments were carried out at 34 °C.

Multi-spectral Optoacoustic Tomography

Ex vivo and animal MSOT measurements (Figure S1A) were conducted with a 256-channel real-time imaging MSOT scanner (Dima et al., 2014) (inVision 256-TF, iThera Medical GmbH, Munich, Germany) using a tunable (680-950 nm) pulsed (<10 ns) optical parametric oscillator laser with a 10 Hz repetition rate. A fiber bundle split in 10 output arms was used for homogeneous light delivery to the imaged sample along a line illumination around the animal body (ring-shaped illumination). Optoacoustic signals were simultaneously acquired by a 256-element, cylindrically focused transducer array covering a solid angle of 270° around the imaged object. The individual detector elements were manufactured from piezocomposite material and had a central frequency of 5 MHz. The system can acquire cross-sectional (transverse) images through phantoms or small animals like mice. A moving stage enables the imaging of different planes, while the illumination and detection devices remain static.

Indirect Calorimetry

Oxygen consumption for each mouse was analyzed continuously during MSOT scanning using a transportable O₂ analyzer (FoxBox, Sable Systems International, USA). Air at atmospheric pressure was supplied by means of a compressed air bottle reservoir. For the analysis of gas concentrations, air was pulled through the MSOT sample holder using the pump included in the FoxBox respirometry system with a flow rate of 800 ml/min. After leaving the sample holder, air was dehumidified by passing through a cooling trap and then a tube with magnesium perchlorate (Merck KGaA, Germany). Air was then filtered (Model 9922-11, Parker Balston) before entering the O₂ analyzer (Figure S1A). To correct for drift in the data, the air was pulled through the empty animal holder before and after the analysis of the mouse (baseline measurement). Drift correction was performed using the software ExpeData, which was also used for data recording (ExpeData version 1.1.22, Sable Systems International, USA). Data were collected in 1-sec intervals. Oxygen consumption ($\dot{V}O_2$) of the mouse was calculated according to the following equation (Heldmaier and Ruf, 1992): $\dot{V}O_2$ [ml/h] = $\Delta vol\%O_2 \cdot 10 \cdot flow$ [l/h]. Four mice were analyzed for the activation experiment (norepinephrine injection) and three mice were used as controls (saline injection).

Mouse MSOT Measurements Ex Vivo

Ex vivo measurements were performed to measure BAT and WAT spectra and interrogate whether these two different types of tissue could be spectrally separated in tissue-mimicking phantoms. Interscapular BAT and inguinal WAT from the hind limb were collected from mice, perfused with 5 ml PBS and inserted into 3-mm diameter plastic tubes. The 3-mm tubes were then embedded into a 2-cm diameter cylindrical phantom made of 1.3% agar (Sigma-Aldrich, St. Louis, MO, USA) and 6% intralipid emulsion (Sigma-Aldrich, St. Louis, MO, USA), leading to an optically diffusive medium with acoustic properties similar to those of tissue. The use of diffusive phantoms enables better simulation of the geometry, illumination conditions, and acoustic detection conditions expected *in vivo* (Vonnemann et al., 2014). Imaging was performed at 21 wavelengths in the range 700 nm - 900 nm in steps of 10 nm. For referencing purposes, a previously characterized tube containing India ink was also measured. The ink solution yielded an optical density of 0.5, as determined by a spectrophotometer. MSOT imaging experiments were carried out at 34 °C.

Mouse MSOT Measurements In Vivo

Mice were anesthetized by i.p. injection of 75 mg/kg pentobarbital and placed in the MSOT sample holder as described earlier (Razansky et al., 2011). In brief, all animals were placed onto a thin, clear, polyethylene membrane and positioned in the water bath maintained at 34 °C, which provided acoustic coupling and maintained animal temperature while imaging. For imaging BAT activation, norepinephrine (arterenol, Sanofi, Germany; 1 mg/kg; Meyer et al., 2010) was injected via a catheter inserted in the tail vein. A total of six animals were used for the activation experiments. Three control animals were injected with saline (0.9 % NaCl). In each measurement, 10 wavelengths spanning 700 nm to 900 nm were acquired in 20-nm steps. The duration of anesthesia and MSOT acquisition was limited to ~2500 sec to ensure ethical animal treatment. MSOT imaging experiments were carried out at 34 °C.

Cryoslicing

After imaging, the mice were euthanized with a lethal dose of pentobarbital and frozen to -50 °C. The upper torso including the neck was embedded in O.C.T (TissueTeck; Sakura Finetek, USA) and was transversely cryosliced with a step of 50 micrometers at -20 °C using a modified cryotome (CM 1950; Leica Microsystems, Germany) equipped with a CCD camera. The camera was used to capture RGB color images of the surface of the bulk sample remaining after each slicing cycle (Tzoumas et al., 2014).

Model-Based Reconstruction and Data Analysis

A model-based tomographic reconstruction method, previously described (Rosenthal et al., 2010), was employed for MSOT image formation. Optoacoustic images obtained at different wavelengths were then linearly unmixed for oxy- (HbO₂) and deoxygenated (Hb) hemoglobin (in the 700-900 nm) and fat and water (in the 900-970, when available). Hemoglobin values were normalized against

the maximum HbO₂ value measured in an artery selected for normalization purposes. The data analysis further consisted of the calculation of the total blood volume (TBV = HbO₂ + Hb, displayed as arbitrary unit) and the oxygen saturation (SO₂ = HbO₂ / TBV, displayed as percentage), the latter closely relating to tissue oxygenation and metabolic changes over time. SO₂ was also calibrated based on an artery signal, assumed to reflect 100% oxygen saturation. SO₂ and TBV rates were drawn by calculating the 1st derivative of the SO₂ and TBV over time. Calculation of activation areas (contour maps; [Figures S3A–S3D](#)) was based on discretizing the HbO₂ and Hb images, before and after activation, down to 5 intensity levels. In animal studies always both BAT depots were used to calculate the HbO₂, Hb, TBV and SO₂. For data analysis the procedures were not done blinded.

MSOT Handheld Measurements and Indirect Calorimetry in Human Subjects

¹⁸F-FDG-PET and MRI data (Biograph mMR; Siemens Healthcare, Germany) from three subjects were acquired at 70–158 min after the injection of 320–408 MBq ¹⁸F-FDG. MRI images were co-registered on the PET images using fiducial markers. To visualize BAT and measure its activation in humans, a handheld MSOT was used as described previously ([Dima et al., 2014](#); [Diot et al., 2015, 2017](#)). The scanner was based on a 4.5-cm radius semi-circular detector interfaced to human tissue through a water-containing chamber. The handheld MSOT illumination was provided by a tunable pulsed laser (Spotlight 600 OPO, Innolas Laser GmbH, Germany) capable of wavelength tuning (675–1064 nm) on a per-pulse basis at 50 Hz repetition rate. The light was coupled into a fiber bundle (CeramOptec GmbH) with rectangular output size of 40-by-1 mm² to create a line illumination. For detection, a multi-element piezoelectric transducer was used with 256 elements placed in a half arc of 120-mm diameter and central frequency of 5 MHz ([Figure S1B](#)). All imaging experiments were carried out at room temperature (20–25°C).

For BAT activation measurements, three subjects wore a cooling suit (EOD cooling suit with pump assembly, Holdfast Systems, ZA). The cooling suit comprises a one-piece garment covering the upper body, upper arms and legs, as well as a close-fitting, open-faced hood for the head as well as a cooling pump that circulates ice-cooled water (13 °C) through hoses integrated in the garment. The duration of the cooling was 20 minutes and was terminated when the subject started to shiver. During MSOT handheld imaging, the oxygen consumption of the subjects was analyzed continuously using an exercise physiology kit (ML3508B80 Exercise Physiology System, ADInstruments, NZ). IC data were collected at a rate of 1000 Hz and analyzed by LabChart software (LabChart7 version v.7.2, ADInstruments, NZ) to calculate the oxygen consumption ($\dot{V}O_2$ [L/min]), which is presented as a moving average over 20 points.

MRI –MSOT Correlation in Human Subjects

Ten healthy adult volunteers (6 male, 4 female; mean age 35), were recruited prospectively. Subjects underwent an MRI of the neck region on a 3T scanner (Ingenia, Philips Healthcare). For measuring the supraclavicular proton density fat fraction (PDFF) ([Baum et al., 2016](#); [Hu and Kan, 2013](#)), a six-echo multi-echo gradient echo sequence with bipolar gradients was used with TR = 12 ms, TE1 = 1.24 ms, $\Delta TE = 1.0$, flip angle = 5°, bandwidth = 1413 Hz/pixel, 268x200x93 acquisition matrix size, FOV = 400x300x140 mm³, 1.5-mm isotropic voxel size, and SENSE with R = 2.5. PDFF maps were generated using the online complex-based fat quantification algorithm, accounting for known confounding factors including the presence of multiple fat peaks, a single T2* correction and phase errors ([Baum et al., 2016](#); [Hu and Kan, 2013](#); [Karampinos et al., 2011, 2014](#)). A custom-built MATLAB algorithm was used for delineating the left deep supraclavicular fat pocket and determining the mean supraclavicular PDFF.

MSOT images of approximately the same region were recorded in an extended 700–970 nm spectral region, with the same system discussed in the previous section. For the reproducibility study one subject with confirmed BAT (by MRI-PDFF) was scanned 10 times on the right and 10 times on the left supraclavicular region. In all subjects, ROIs from supraclavicular regions expected to contain BAT or WAT were employed to unmix for fat content (presence of fat spectral intensity in total MSOT spectrum) and water content (presence of water spectral intensity in total MSOT spectrum), utilizing the 900–970 nm spectral window, which contains prominent absorption contributions from lipids and water.

To detect BAT in humans and distinguish it from WAT using MSOT data, we generated maps of blood and fat distribution by recording a multi spectral image, taken at 28 different wavelengths (700 to 970 nm), and extracted the Hb and HbO₂ distribution from a fit of the measured spectra in the 700 to 900 nm range to the known absorption spectra of Hb and HbO₂. The amount of blood (i.e. total blood volume TBV) was computed from $[TBV] = [Hb] + [HbO_2]$ for each pixel. The distribution of lipids was extracted by fitting spectra in the 700 to 970 nm range to Hb, HbO₂, fat and water. Based on the distribution of lipids and the depth estimate of the BAT region from MRI (~ 1.5 cm), we segmented a deeper-lying fat area. For further characterization of this area, we analyzed the spectral heterogeneity of pixels at the expected depths of BAT in the supraclavicular region regarding their intensity in blood and fat amplitudes. A high fat and low blood population and a high blood and lower fat population were identified in a plot of the unmixed blood and lipids amplitude of each pixel at the expected depths of BAT in the supraclavicular region. Moreover, the spatial positions were identified and highlighted on the anatomic image which clusters them in two different regions. The mean spectrum of the two clusters exhibits distinct differences regarding their blood content (700 to 900 nm) compared to the fat peak at 930 nm.

The MSOT fat fraction (MSOT-FF) was computed as the fat spectral intensity over fat and water spectral intensity. The MSOT blood fat fraction (MSOT-BFF) was computed as the total blood volume spectral intensity over fat and total blood volume spectral intensity. The correlation was determined by calculating the Spearman's correlation coefficient. All imaging experiments were carried out at room temperature (20–25°C). For data analysis the procedures were not done blinded.

QUANTIFICATION AND STATISTICAL ANALYSIS

All data are presented as mean \pm SEM and n is indicated for each experiment. Datasets were tested for normal variance and correlations. Depending on the data Student's t -test, or the Spearman's correlation coefficient test were used for comparisons and indicated in the legends of each panel. The data met the assumptions of the statistical approach. A p -value of < 0.05 was considered as statistically significant.

DATA AND SOFTWARE AVAILABILITY

The ultrasound signals recorded per laser pulse and per wavelength were used to produce a planar optoacoustic image via a customized model-based tomographic reconstruction method, already described elsewhere in detail ([Rosenthal et al., 2010](#)). Model-based reconstruction methods do not simply attempt to solve the inverse problem, which means they do not simply attempt to calculate the final optoacoustic image from the recorded ultrasound signals. On the contrary, model-based methods rely on a previously known solution to the forward problem, which means that given an ideal model of the unknown optoacoustic image, the final optoacoustic image is calculated by minimizing an error function between the recorded ultrasound signals and that corresponding to the ideal model. Model-based reconstruction methods can produce quantified optoacoustic reconstructions with much less artifacts compared to traditional approaches.

The acquired multi-spectral data were further unmixed via a linear spectral unmixing algorithm already used in other clinical MSOT applications ([Diot et al., 2017](#)). In this approach, a set of reference absorption spectra in the NIR range (e.g. HbO₂, Hb, lipids, water) are given as input to the algorithm. The recorded spectrum for each pixel of a multi-spectral image is considered to be a linear combination of the reference spectra. Finally, the algorithm assigns a reference absorber to each pixel by fitting a reference spectrum to the measured one. The theoretical background of the custom code employed is already publicly available. The custom code may be provided upon request to the Lead Contact.

Cell Metabolism, Volume 27

Supplemental Information

Non-invasive Measurement of Brown

Fat Metabolism Based on Optoacoustic

Imaging of Hemoglobin Gradients

Josefine Reber, Monja Willershäuser, Angelos Karlas, Korbinian Paul-Yuan, Gael Diot, Daniela Franz, Tobias Fromme, Saak V. Ovsepian, Nicolas Bézière, Elena Dubikovskaya, Dimitrios C. Karampinos, Christina Holzapfel, Hans Hauner, Martin Klingenspor, and Vasilis Ntziachristos

Figure S1 – Experimental setup

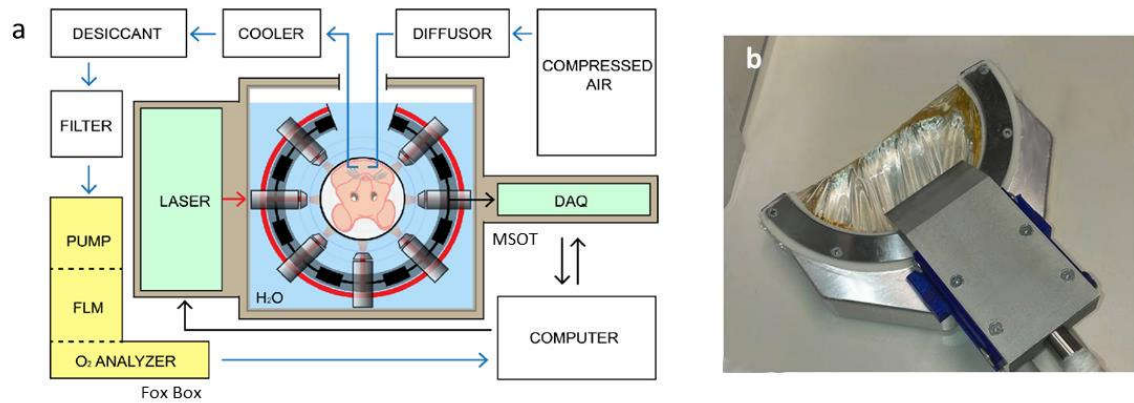


Figure S1, related to all Figures. Experimental setups. (a) Schematic overview of the experimental setup, showing the small-animal MSOT imaging system (black lines) and the indirect calorimetry system (blue lines) based on the FoxBox. (b) Handheld MSOT imaging probe with illumination and sealed water coupling connected.

Figure S2 – Comparison between diabetic and healthy mice

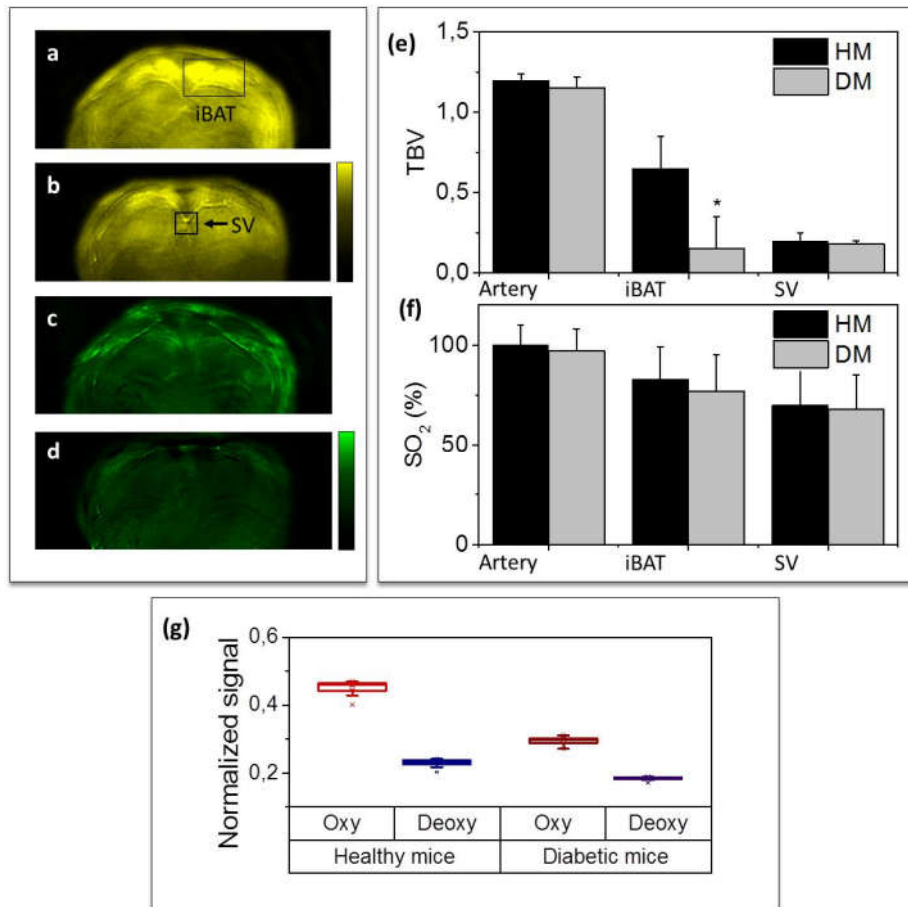


Figure S2, related to Figure 1. Comparison of interscapular brown adipose tissue (iBAT) area in healthy BALB/c mice (HM) and in mice with streptozotocin-induced diabetes (DM) by means of MSOT *in vivo*. (a) Unmixed MSOT image of total blood volume (TBV) in HM showing interscapular BAT (iBAT) (black box). (b) Unmixed MSOT image of TBV in DM. The Sulzer Vein (SV) is indicated by a black box and arrow. (c) Unmixed MSOT image of blood oxygen saturation (SO₂) in HM. (d) Unmixed MSOT image of SO₂ in DM. (e) Normalized signal of TBV in a reference artery, the iBAT and Sulzer vein (SV) in HM and DM. (f) Normalized SO₂ signal intensity in a reference artery, the iBAT and Sulzer vein (SV) in HM and DM. (g) Mean normalized signal intensity of HBO₂, HB in HM and DM. (*p < 0.05). Data are represented as mean ± SEM.

Figure S3 – BAT area implicated in activation

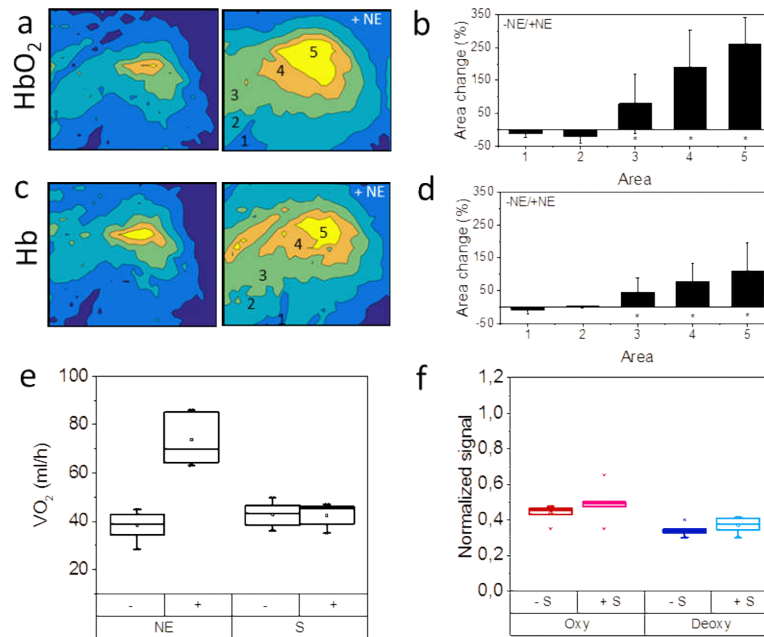


Figure S3, related to Figure 2. Brown adipose tissue (BAT) activation. (a) Changes of five intensity areas of oxygenated hemoglobin (HbO₂) in the right interscapular BAT (iBAT) lobe before and after activation with norepinephrine (NE). (b) Percentage changes within the five intensity areas after activation. (c) Changes of five intensity areas of deoxygenated hemoglobin (Hb) in the right iBAT lobe before and after activation with NE. (d) Percentage changes in the five intensity areas after activation. (e) Indirect calorimetry readouts of oxygen consumption in animals (VO₂) before and after NE or saline (S) injections. (f) MSOT signal of HbO₂ and Hb before and after saline (S) injections as a control experiment. Data are represented as mean ± SEM.

Figure S4 – BAT activation in humans

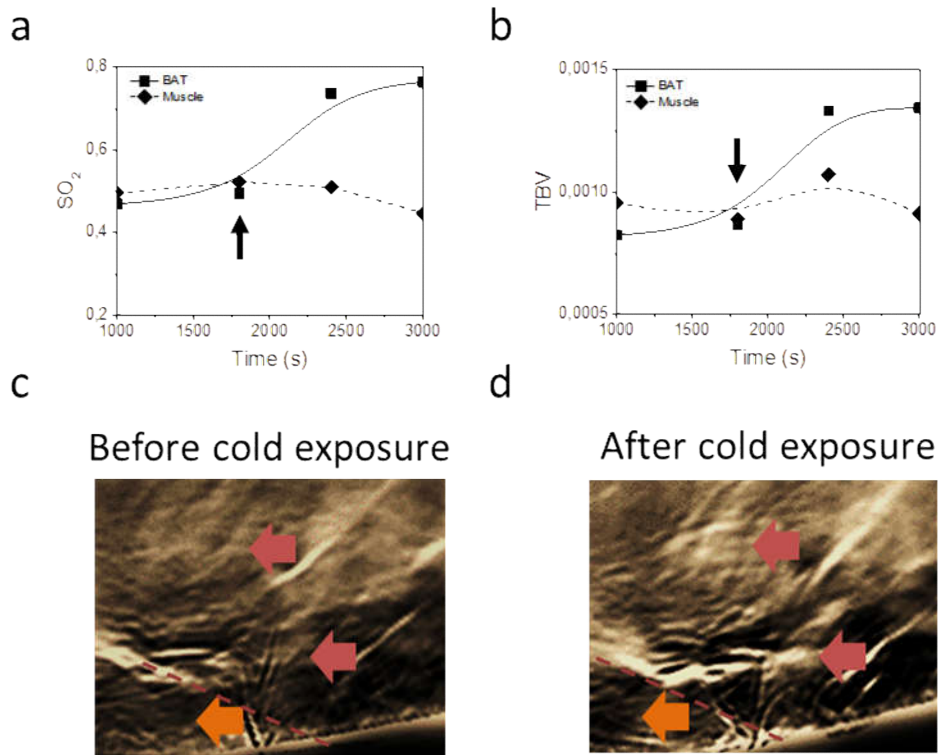


Figure S4, related to Figure 5. MSOT handheld optoacoustic signals measured in volunteers. (a) Blood saturation (SO_2) in brown adipose tissue (BAT) and muscle. (b) Total blood volume in brown adipose tissue (BAT) and muscle. Cold exposure ($13\text{ }^{\circ}\text{C}$) started after 1800 s (black arrow). (c,d) Images obtained from the supraclavicular region of a healthy volunteer before (c) and after (d) cold exposure. Red arrows indicate areas of activation in the BAT region; the orange arrow shows a muscle area that did not exhibit a significant intensity change before and after activation.

Figure S5 -Hb, HbO₂, Fat and Water imaging of BAT in human volunteers

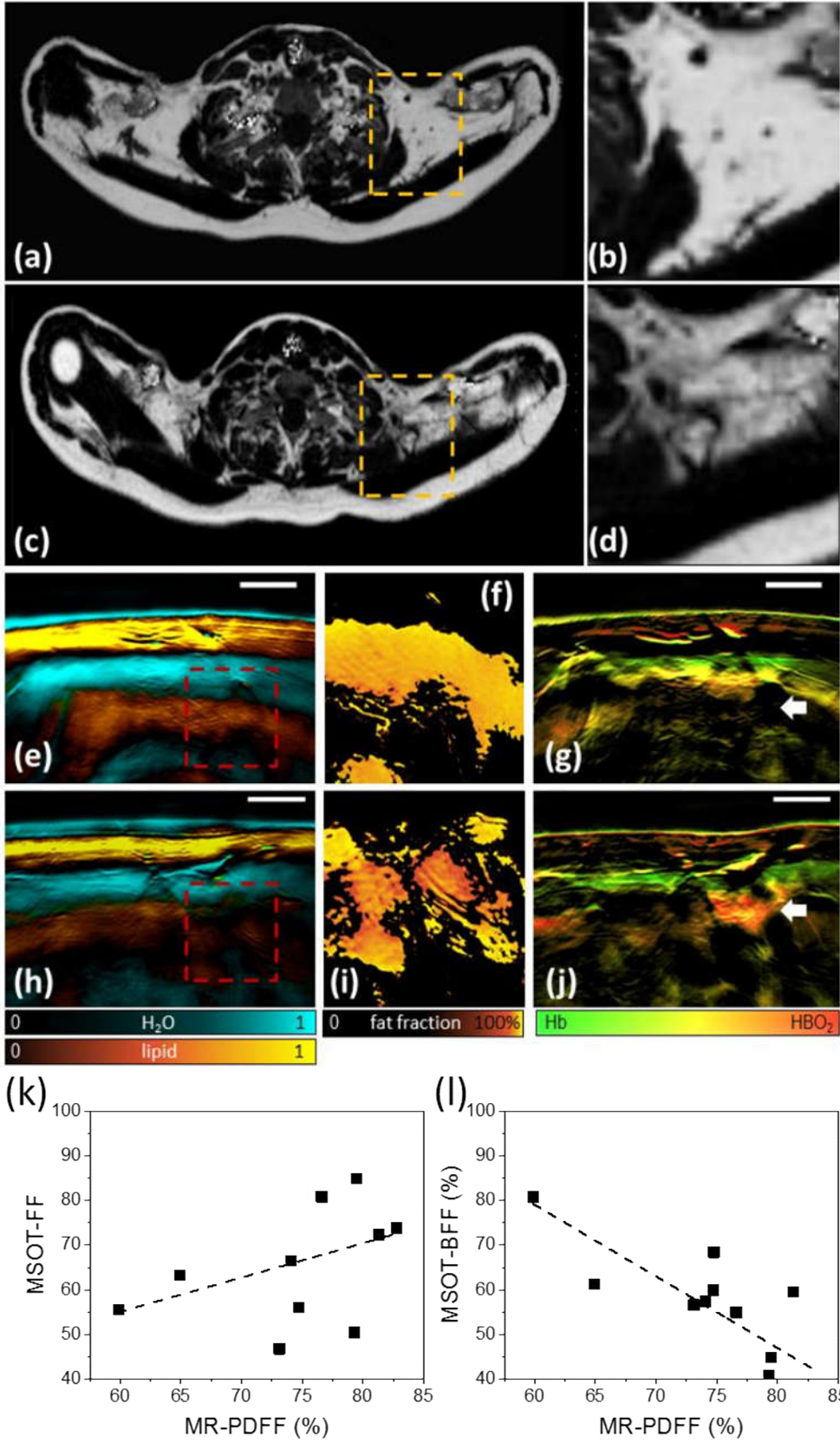


Figure S5, related to Figure 5. MRI and MSOT imaging of brown adipose tissue (BAT) at the basal state in human volunteers. (a) MRI image of a volunteer with high PDFF (83%) in the region of interest (ROI) contained within the yellow rectangle. (b) Zoomed-in picture of ROI in the yellow rectangle. (c,d) Images corresponding to panels a and b from a volunteer exhibiting a low PDFF value (68%) extending over a smaller area than in panel a, indicative of BAT presence. (e) MSOT image showing water and lipid concentrations from the volunteer in panel a. (f) MSOT fat fraction from the area delineated by a red rectangle in panel e, depicting virtually 100% lipid concentration. (g) MSOT image of the oxy- and deoxy-hemoglobin concentrations corresponding to panel e. (h) MSOT image of water and lipid obtained from the volunteer in panel c, demonstrating reduced lipid in the same area as the one shown in panel d. (i) MSOT fat fraction of the area indicated by a red rectangle in panel h, demonstrating lower FF than in panel f. (j) MSOT image of Hb and HbO₂ from the volunteer in panel c shows increased vascularization in an area consistent with reduced lipid content, indicative of the presence of brown fat. (k) Correlation analysis between MSOT-FF and MRI-PDFF across 10 adult volunteers, showing a Spearman's correlation coefficient of 0.55 ($p = 0.04$); linear regression marked with the dashed line. (l) Correlation analysis between MSOT-BFF and MRI-PDFF across 10 adult volunteers, showing a Spearman's correlation coefficient of -0.69 ($p = 0.02$); linear regression marked with the dashed line. Scale bars 1 cm.

Table S1

Table S1, related to Figure 1. Comparison of healthy and diabetic mice by means of MSOT. Blood glucose and body weight measured at the day of MSOT measurement 3 weeks after induction of diabetes via streptozotocin injection in male balb/c mice (n=3). Length and depth of iBAT region determined *in vivo*. ROI defined in the iBAT region of each animal on both iBAT lobes and mean signal intensity calculated in the ROI after image reconstruction.

	Blood glucose level (mg/dl)	Body weight (g)	iBAT weight (g)	ROI (mm²)	ROI mean signal intensity	iBAT length (mm)	iBAT depth (mm)
Healthy animals	142 ± 3	40.8 ± 2	0.20 ± 0.04	~ 1.6	97 ± 11	6.5 ± 1.3	1.6 ± 0.1
Diabetic animals	> 600*	41.4 ± 3	0.18 ± 0.05	~ 1.6	80 ± 18*	5.0 ± 1.1	1.2 ± 0.1*

*p<0.05